

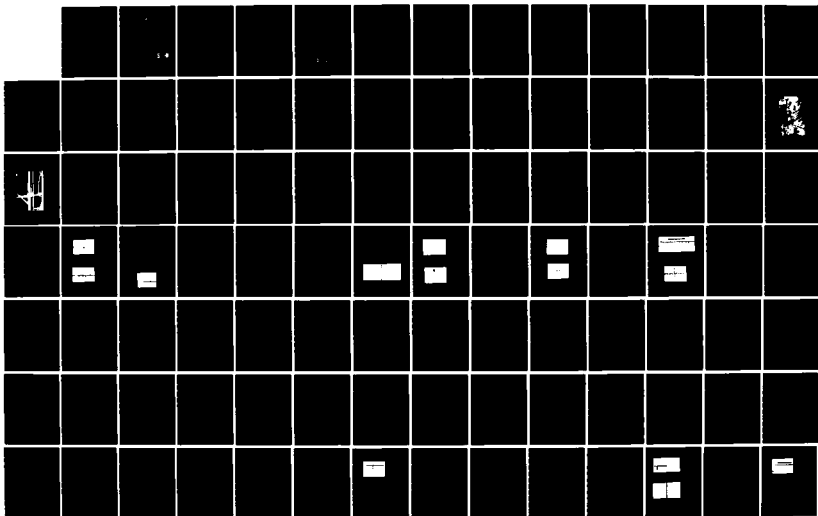
AD-A154 694

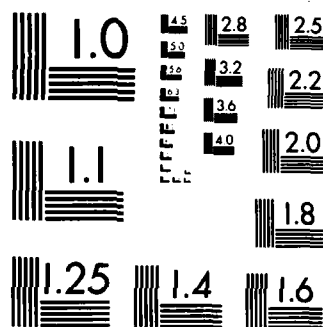
VELOCITY AND TRANSIENT MEASUREMENTS IN A SHOCK TUBE
USING A HOT-WIRE ANEMOMETER(U) AIR FORCE INST OF TECH
WRIGHT-PATTERSON AFB OH SCHOOL OF ENGI... S H MCQUEEN
DEC 84 AFIT/GAE/AA/84D-17 F/G 14/2

1/2

UNCLASSIFIED

NL





MICROCOPY RESOLUTION TEST CHART
NATIONAL BUREAU OF STANDARDS-1963-A

1

AD-A154 694



VELOCITY AND TRANSIENT MEASUREMENTS
IN A SHOCK TUBE USING A HOT-WIRE
ANEMOMETER

THESIS

Stephen M. McQueen
Captain, USAF

AFIT/GAE/AA/84D-17

Accessi

NTIS G

DTIC TA

Unannon

Justifi

By

This document has been approved
for public release and sale; its
distribution is unlimited.

DEPARTMENT OF THE AIR FORCE
AIR UNIVERSITY

AIR FORCE INSTITUTE OF TECHNOLOGY

DTIC
ELECTE
S **D**
E

Wright-Patterson Air Force Base, Ohio

85 5 06 169

DTIC FILE COPY

UNCLASSIFIED

SECURITY CLASSIFICATION OF THIS PAGE

REPORT DOCUMENTATION PAGE

1. REPORT SECURITY CLASSIFICATION UNCLASSIFIED			1b. RESTRICTIVE MARKINGS		
2a. SECURITY CLASSIFICATION AUTHORITY			3. DISTRIBUTION/AVAILABILITY OF REPORT Approved for public release; distribution unlimited.		
2b. DECLASSIFICATION/DOWNGRADING SCHEDULE					
4. PERFORMING ORGANIZATION REPORT NUMBER(S) AFIT/GAE/AA/84D-17			5. MONITORING ORGANIZATION REPORT NUMBER(S)		
6a. NAME OF PERFORMING ORGANIZATION School of Engineering		6b. OFFICE SYMBOL (If applicable) AFIT/ENG		7a. NAME OF MONITORING ORGANIZATION	
6c. ADDRESS (City, State and ZIP Code) Air Force Institute of Technology Wright-Patterson AFB, Ohio, 45433				7b. ADDRESS (City, State and ZIP Code)	
8a. NAME OF FUNDING/SPONSORING ORGANIZATION		8b. OFFICE SYMBOL (If applicable)		9. PROCUREMENT INSTRUMENT IDENTIFICATION NUMBER	
8c. ADDRESS (City, State and ZIP Code)				10. SOURCE OF FUNDING NOS.	
				PROGRAM ELEMENT NO. PROJECT NO. TASK NO. WORK UNIT NO.	
11. TITLE (Include Security Classification) see box 19 - UNCLASSIFIED					
PERSONAL AUTHOR(S) Stephen M. McQueen, B.S., Captain, USAF					
13a. TYPE OF REPORT M.S. Thesis		13b. TIME COVERED FROM TO		14. DATE OF REPORT (Yr., Mo., Day) 1984 December	
15. PAGE COUNT 117					
16. SUPPLEMENTARY NOTATION					
17. COSATI CODES			18. SUBJECT TERMS (Continue on reverse if necessary and identify by block number)		
FIELD	GROUP	SUB. GR.			
04	02		Shock Tube, Hot-Wire Anemometry; Turbulence; Karman Vortex Street.		
19. ABSTRACT (Continue on reverse if necessary and identify by block number)					
TITLE: VELOCITY AND TRANSIENT MEASUREMENTS IN A SHOCK TUBE USING A HOT-WIRE ANEMOMETER (UNCLASSIFIED)					
THESIS CHAIRMAN: Dr. William C. Elrod					
Approved for public release: IAW AFR 190-1 18 APR 85 Wright-Patterson AFB OH 45433					
20. DISTRIBUTION/AVAILABILITY OF ABSTRACT UNCLASSIFIED/UNLIMITED <input checked="" type="checkbox"/> SAME AS RPT. <input type="checkbox"/> DTIC USERS <input type="checkbox"/>			21. ABSTRACT SECURITY CLASSIFICATION UNCLASSIFIED		
22a. NAME OF RESPONSIBLE INDIVIDUAL Dr. William C. Elrod			22b. TELEPHONE NUMBER (Include Area Code) 513-255-3517		22c. OFFICE SYMBOL AFIT/ENY

Log of the investigation

This investigation explored the suitability of the TSI IFA-100 Intelligent Flow Analyzer system, with TSI 1210 and 1214-T1.5 hot-wire sensors, to measure the velocity behind the incident shock wave in a shock tube. Additionally, velocity fluctuations as a result of Kármán vortex street formation behind a 3/16-inch cylinder were also measured. The range of Reynolds numbers was $23,000 < Re < 35,000$ in this configuration.

Calibration of the hot-wire was accomplished from ambient temperature to 275°F with individual calibrations at discrete temperatures (ie. 74°F, 175°F, 275°F) designed to cover the expected test conditions up to 200°F and 620 ft/s. Velocities measured ranged from 312 to 590 ft/s with 4 percent or better accuracy. Velocity fluctuations were measured and computed as turbulence intensities, and ranged from 1.75 to 9.52 percent.

The results of the investigation showed favorable indication that velocity can be measured with reasonable accuracy in a shock tube with the IFA-100 system. *recovery*

Stephen M. McQueen
Captain, USAF

DTIC
ELECTE
JUN 4 1985

Accession For	
NTIS GRA&I	<input checked="checked" type="checkbox"/>
DTIC TAB	<input type="checkbox"/>
Unannounced	<input type="checkbox"/>
Justification	
By	
Distribution/	
Availability Codes	
Dist.	Avail and/or Special



AFIT/GAE/AA/84D-17

VELOCITY AND TRANSIENT MEASUREMENTS IN A
SHOCK TUBE USING A HOT-WIRE ANEMOMETER

THESIS

Presented to the Faculty of the School of Engineering
of the Air Force Institute of Technology
Air University
In Partial Fulfillment of the
Requirements for the Degree of
Master of Science in Aeronautical Engineering

Stephen M. McQueen, B.S.
Captain, USAF

December 1984

Approved for public release; distribution unlimited

PREFACE

The purpose of this thesis was to extend the application of the hot-wire anemometer to measurement of high-speed flows found in the shock tube. Throughout the research, a number of related problems surfaced but were of a nature requiring an entire study devoted to solving that particular problem. Two most notable were (a) the structural dynamic problems, including vibration, associated with hot-wire probes when impulsively excited, and (b) heat transfer errors due to probe prongs and supports not coming to the gas flow temperature as was the case during steady flow calibration. This work should be continued, as it could be of significant value in providing information leading to a more universal method of hot-wire calibration.

I wish to sincerely thank the great number of people who, after the many long hours of preparation and experimentation, made this thesis possible.

Sincere appreciation is extended to Professor William C. Elrod as my thesis advisor, and to Dr. Richard B. Rivir of the Aero Propulsion Laboratory for their valuable assistance and cooperation in the successful completion of this study. Appreciation is also extended to Captain (Dr.) Wesley Cox and Dr. James E. Hitchcock for their timely assistance and advice throughout this project. A

special acknowledgement is made to Mr. Nickolas Yardich, Mr. H.L. Cannon, Mr. Harley Linville, Mr. Carl Shortt, Mr. Ron Ruley, and Mr. Russell Murray, for their technological expertise in the experimental set up. Finally I wish to express love and thanks to my wife, Lorri, for her patience and sacrifices throughout this research.

Stephen McQueen

Table of Contents

	<u>Page</u>
Preface	ii
List of Figures	vi
List of Tables	x
List of Symbols	xi
Abstract	xiv
I. Introduction	1
Purpose and Scope	2
II. Shock Tube Operation	3
Shock Tube	3
Shock Tube Assembly	6
General Description	6
Dump Tank	7
Diaphragm Section	7
Test Section	10
Air Supply	11
III. Theory of Hot-Wire Operation and Calibration	13
Theory of Operation	13
Calibration	16
General	16
Hot-Wire Anemometer Calibrator	17
IV. Calibration and Test Procedure	20
Calibration	20
Pressure Transducers	20
Hot-Wire Anemometer Calibrator	20
Measurement Procedures	22
Frequency Response	23
V. Data Reduction	25
Shock Velocity	25
Pressure	25
Temperature	27
Air Velocity	27
Kármán Vortex Streets	31

	<u>Page</u>
VI. Discussion of Results	36
Calibration	36
Shock Tube Experiment	57
Velocity	57
Kármán Vortex Streets	66
Pressure	71
Mylar Burst Phenomenon	72
Hot-Film Mechanical Resonance	77
VII. Conclusions and Recommendations	79
Conclusions	79
Recommendations	80
Appendix A: Instrumentation	82
Appendix B: Hot-Film Mechanical Resonance	86
Appendix C: Test Data	89
Bibliography	98
Vita	100

List of Figures

<u>Figure</u>	<u>Page</u>
1. Shock Tube Operating Conditions	5
2. Shock Tube Used During Testing	8
3. Test Section Showing Proximity of Hot-Wire Probe to the Cylinder	9
4. Schematic of Test Section Showing Hot-Wire Probe and Transducer Locations	12
5. Schematic of Calibrator Used to Calibrate Hot-Wire Probes	18
6. Photograph of an Oscilloscope Trace Showing the Frequency Response of the Hot-Wire at 400 ft/s . .	24
7. Photograph of an Oscilloscope Trace Showing the Frequency Response of the Hot-Wire at 810 ft/s . .	24
8. Photograph of an Oscilloscope Trace Showing Pressure Rise After Shock Wave Passage	25
9. Photographs of Anemometer Output Signals Showing (9a) Output Directly to an Oscilloscope, and (9b) Input to a Transient Response Recorder Before Output to an Oscilloscope	29
10. Photograph of an Oscilloscope Trace Showing Anemo- meter Output for the Highest Velocity Tested . . .	30
11. Photograph of an Oscilloscope Trace Showing Anemo- meter Output for the Highest Velocity Tested . . .	30
12. Photographs of Oscilloscope Traces Showing the Initial Part of the Hot-Wire Signal as the Shock Wave Passes the Probe	32
13. Photograph of an Oscilloscope Trace Showing the Anemometer Signal Captured by a Transient Response Recorder	34
14. Photograph of an Oscilloscope Trace Showing Increased Voltage Sensitivity	34
15. Calibration Plot for Probe 8052 Showing Effect of Prandtl No. Exponents on 61° F Temperature Curve (TREX=-2.7, RXP=0.46, PRXP=1.0, PRX2=1.0).	41

16. Calibration Plot for Probe B052 Showing Effect of Prandtl No. Exponents on 61° F Temperature Curve (TREX=-2.7, RXP=0.46, PRXP=.9, PRX2=0.2)	42
17. Ideal Variation of Nusselt No. (E_o^2) with Reynolds No. (Velocity) as Temperature Changes .	44
18. Hot-Wire Calibration Plot for Probe K481 Showing 74° F, 175° F, and 275° F Temperature Ranges (TREX=-4.0, RXP=0.49, PRXP=1.0, PRX2=1.0)	45
19. Hot-Wire Calibration Plot for Probe K481 Showing 74° F, 175° F, and 275° F Temperature Ranges (TREX=1.0, RXP=0.49, PRXP=1.0, PRX2=1.0)	46
20. Hot-Wire Calibration Plot for Probe K481 Showing 74° F, 175° F, and 275° F Temperature Ranges (TREX=0, RXP=0.5 PRXP=0.2, PRX2=0.9)	47
21. Hot-Wire Calibration Plot for Probe K481 Showing 74° F, 175° F, and 275° F Temperature Ranges in "Collapsed-Linear" Form (TREX=-2.03, RXP=0.49 PRXP=0.2, PRX2=0.9)	49
22. Hot-Wire Calibration Plot for Probe K481 Showing 74° F Temperature Range (TREX=-2.03, RXP=0.49 PRXP=1.0, PRX2=1.0)	50
23. Hot-Wire Calibration Plot for Probe K481 Showing 175° F Temperature Range (TREX=-2.03, RXP=0.49 PRXP=0.2, PRX2=0.9)	51
24. Hot-Wire Calibration Plot for Probe K481 Showing 275° F Temperature Range (TREX=-2.03, RXP=0.49 PRXP=0.2, PRX2=0.9)	52
25. Hot-Wire Calibration Plot for Probe B052 Showing 61° F and 175° F Temperature Ranges in "Collapsed-Linear" Form (TREX=-2.7, RXP=0.46, PRXP=0.5, PRX2=0.8)	54
26. Hot-Wire Calibration Plot for Probe B052 Showing 61° F (TREX=-2.7, RXP=0.46, PRXP=0.5, PRX2=0.8 . .	55
27. Hot-Wire Calibration Plot for Probe B052 Showing 175° F (TREX=-2.7, RXP=0.46, PRXP=0.5, PRX2=0.8 .	56
28. Hot-Wire Calibration Plot for Probe K481 Showing 74° F, 175° F, and 275° F Temperature Ranges (TREX=1.0, RXP=0.49, PRXP=1.0, PRX2=1.0)	59
29. Hot-Wire Calibration Plot for Probe K481 Showing 74-275° F Temperature Range Ready for Interpolation (TREX=1.0, RXP=0.49, PRXP=1.0, PRX2=1.0)	59

30. Hot-Wire Calibration Plot for Probe B052 Showing 61°F and 175°F Temperature Ranges (TREX=0, RXP=0.46, PRXP=0.5, PRX2=0.8)	60
31. Hot-Wire Calibration Plot for Probe B052 Showing 61-175°F Temperature Range Ready for Interpolation (TREX=0, RXP=0.46, PRXP=0.5, PRX2=0.8)	60
32. Velocity of Air Behind Incident Shock Wave Measured by Hot-Wire (Collapsed-Linear Calibration) Compared to Actual Velocity	61
33. Velocity of Air Behind Incident Shock Wave Measured by Hot-Wire (Interpolated Calibration) Compared to Actual Velocity	62
34. Accuracy of Hot-Wire Measured Velocity (Collapsed- Linear Calibration) vs. Actual Velocity Behind the Incident Shock Wave	63
35. Accuracy of Hot-Wire Measured Velocity (Interpolated Calibration) vs. Actual Velocity Behind the Incident Shock Wave	64
36. Accuracy of Hot-Wire Measured Velocity vs. Actual Velocity Behind the Incident Shock Wave	65
37. Laminar Near-Wake with Single Vortex Street Instability for $300 < Re < 130,000$	67
38. Strouhal Number as a Function of Reynolds Number .	68
39. Nondimensional Frequency vs. Reynolds Number . . .	69
40. Photograph of an Oscilloscope Trace Showing Flow Conditions Behind the Cylinder in the Shock Tube .	71
41. Turbulence Intensity as an Approximation to Velocity Fluctuations Behind the Cylinder in the Shock Tube	73
42. Incident Shock Experimental Pressure Data Compared to Theory (Ref. 2)	74
43. Photograph of Oscilloscope Traces Showing the Mylar Burst Phenomenon	76
44. Photographs of Oscilloscope Traces Showing (44a) Early Stage Perturbation Transition, and (44b) Pronounced Perturbation Due to the Mylar Burst Phenomenon	78

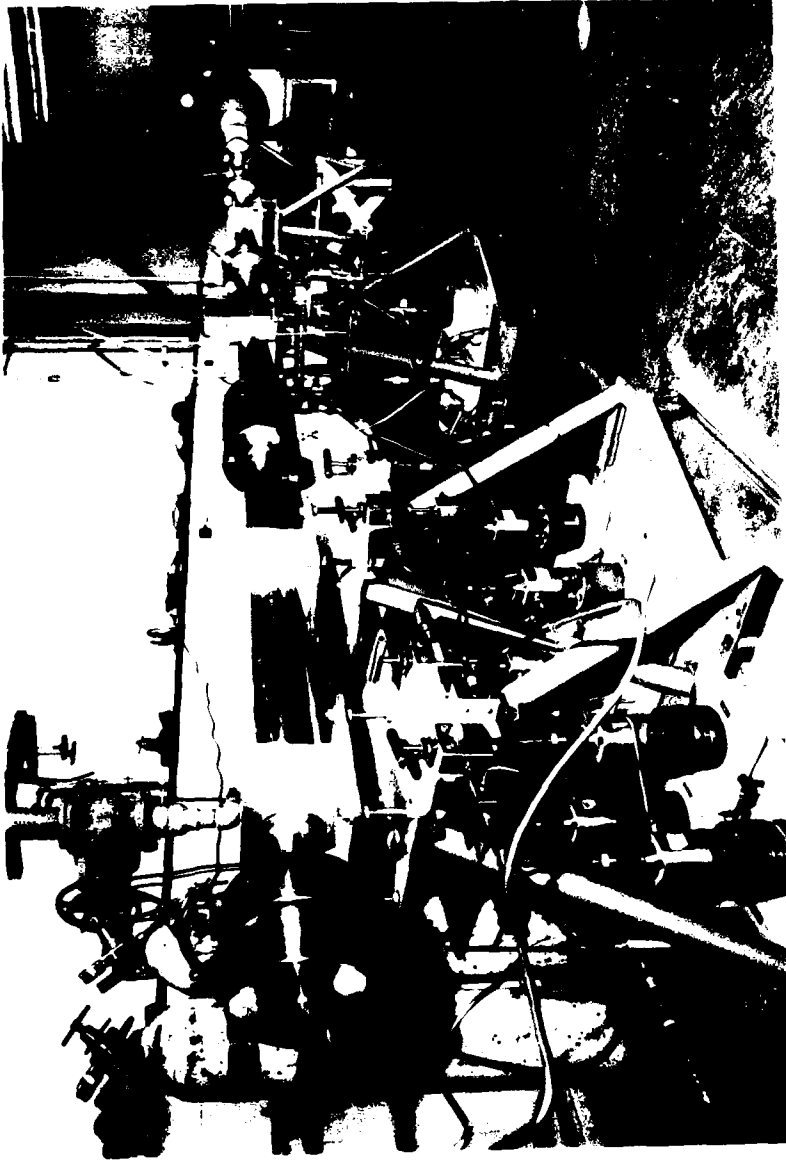


Fig 2. Shock Tube Used During Testing.

assembly was accomplished using a helium-neon laser to verify axisymmetric straightness to within one-sixteenth of an inch. Figures 2 and 3 show the shock tube and test section.

Dump tank. A 400-psia oxygen tank was placed at the end of the driven section so that the shock wave, upon entering this region, would expand and diminish in strength prohibiting a reflected shock wave from propagating upstream into the test section.

Diaphragm Section. The diaphragm assembly used in this shock tube is a jig made to hold one or two diaphragms depending on the operating mode selected. In the single diaphragm mode, raising the driver gas pressure (P_4) to the burst pressure for a given diaphragm material and thickness will rupture the diaphragm and produce a shock wave of strength proportional to P_4/P_1 . This method is suitable for producing shocks but poor for predicting what the shock strength will be when the diaphragm bursts. The double diaphragm mode can be more useful in predicting both shock strength and when the firing of the shock tube is to take place. In the double diaphragm mode, two diaphragms are placed in the jig between driver and driven sections. Diaphragm rupture is controlled by raising the pressure in both the driver section and the region between the two diaphragms to approximately one-half the operating pressure required for establishing

Shock Tube Assembly

General Description. The shock tube used in this research was made of type 321 stainless steel tubing (4:3) of modular construction with variable lengths. It is a 2.069 inch inside diameter circular tube with one inch thick walls. Each tube section is approximately five feet long permitting the user to vary both the ratio of lengths of driver to driven sections and the locations of the test section to meet the specific needs of the test. Available test time once the shock has passed is a function of driver and test gases, driver to test gas pressure ratio (P_4/P_1), and distance of the test section from the diaphragm. All testing was performed using a single driver section, and the shock tube assembly including the driven and test sections was 28.5 feet long. The location of the hot-wire probe was approximately 17 feet from the diaphragm section. For ease of operation, an electrically actuated pneumatic piston/cylinder was used to roll the driver section (on tracks) away from the rest of the shock tube between shock firings to gain easy access for changing diaphragms. The shock tube assembly downstream of the diaphragm section was bolted to the concrete floor once the entire assembly was positioned. Bolting the shock tube prevented movement during operation. Precise alignment was necessary to achieve as close to 1-D flow in the test section as possible. Boresighting of the entire

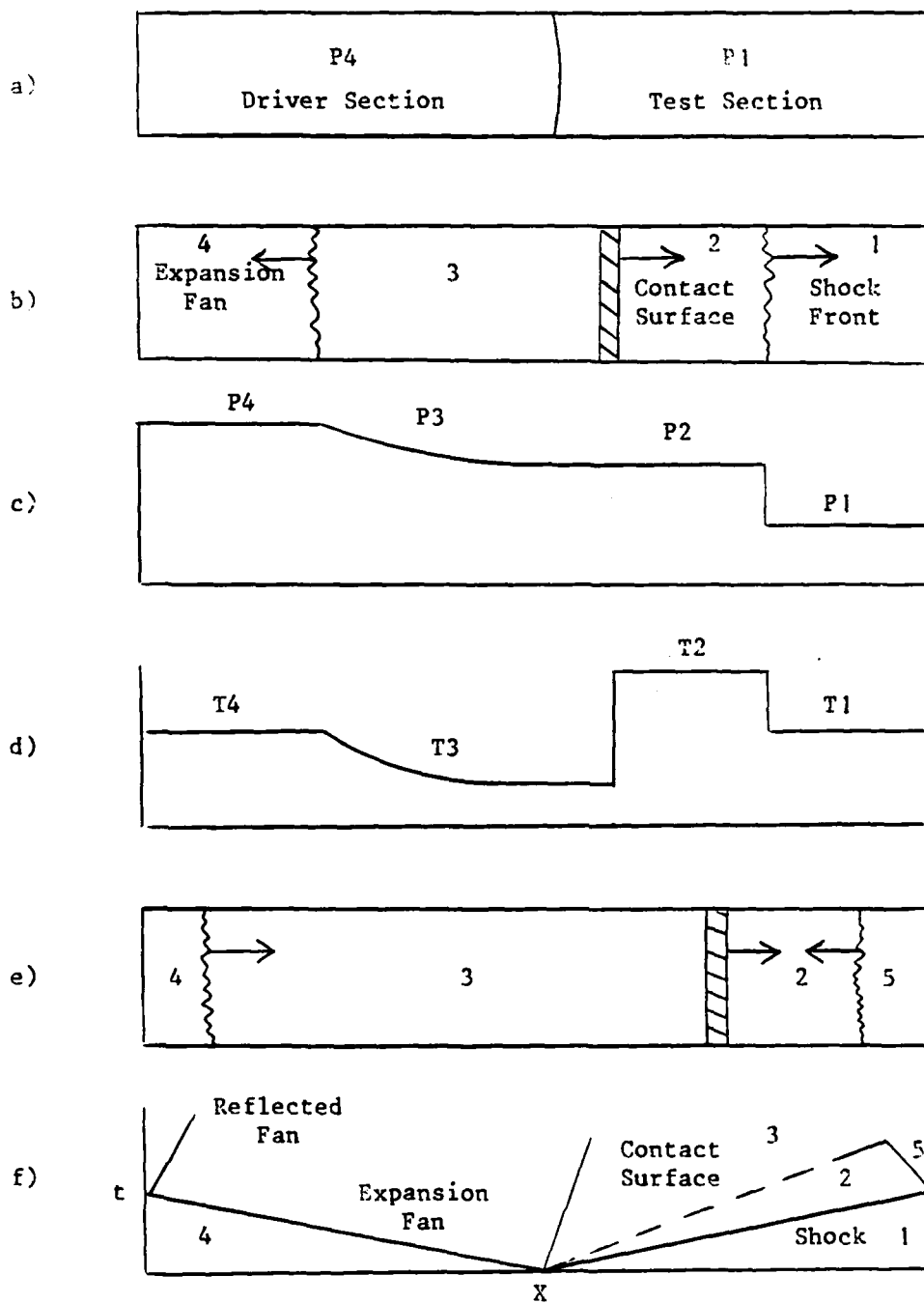


Fig 1. Shock Tube Operating Conditions
(a. Conventional Shock Tube Prior to Diaphragm Rupture; b. After Rupture; c. Pressure Distribution; d. Temperature Distribution; e. After Shock is Reflected Off Tube End; F. Time vs. X Diagram).

purposes of this research, however, the temperature range initially expected to be investigated was from 120° F to 225° F with anticipated shock wave Mach numbers from 1.15 to 1.50 so that air could easily be used as both driver and test gas. A thorough presentation of various gases in shock tube operation is found in reference (3). Additionally, the length of the shock tube and distance of test section from the diaphragm is given as a function of Mach number and test gas in the same reference.

It is usual to denote conditions in the shock tube with the following reference system:

Region 1 - Undisturbed low-pressure experimental gas.

Pressure and temperature are designated as P_1 and T_1 .

Region 2 - The region between the shock front and the contact surface. This is the region of gas in which flow measurements are made.

Region 3 - The region between the contact surface and the rarefaction fan.

Region 4 - The initial conditions at the high-pressure driver section.

Region 5 - The region behind the reflected shock if one were present.

Figure 1 shows these regions and the operating modes of the shock tube.

II. Shock Tube Operation

Shock Tube

The shock tube is a device in which a plane shock wave can be produced by the sudden rupture of a diaphragm which separates a high pressure gas in the driver section from a low pressure gas in the driven section. Immediately after rupture, a compression wave is formed in the low pressure gas which moves into the low pressure driven section and an expansion or rarefaction wave propagates into the high pressure gas. A thin region exists between the driver gas and the "experimental" or driven section gas known as the contact surface, which moves along the tube at the velocity of the gas behind the newly formed shock front. As with any plane shock there is a sharp rise in static temperature and pressure across the shock making the shock tube ideal for establishing a high temperature, high pressure environment where these conditions are required. A limitation is the very short test time available (a few milliseconds) at constant temperature and pressure. The theory of shock tube operation is well documented in Gaydon and Hurle (2) and Glass (3). The magnitude of the pressure rise is governed by the strength of the shock produced. Higher Mach numbers and hence higher strength shocks can be achieved if the driver gas has a high speed of sound and low specific heat ratio (2:20). For the

behind the incident shock wave. Hence, an extension of conventional hot-wire theory is in order, but with possible changes to the basic equations to compensate for these differences. Additionally, the frequency response (1) of the hot-wire anemometer appears to be well suited for shock tube applications, but the impulsive nature of shock passage and instantaneous initiation of velocity raises questions about vibration and structural integrity.

Purpose and Scope

The purpose of this research was to investigate the suitability of a hot-wire anemometer, specifically, a TSI IFA-100 Intelligent Flow Analyzer with the TSI Model 150 anemometer, to measure the velocity behind the incident shock wave in a shock tube. Additionally, turbulence intensity was investigated by measuring time variant velocities with respect to Von Kármán vortex streets produced by flow past a cylinder.

This required calibration of the sensor over the range of velocities, temperatures, and pressures of interest. The shock tube was operated so as to produce temperatures and velocities behind the incident shock wave up to 200 F and 620 ft/s, respectively.

VELOCITY AND TRANSIENT MEASUREMENTS IN A SHOCK TUBE USING A HOT-WIRE ANEMOMETER

I. INTRODUCTION

The hot-wire anemometer has been used for many years as a research tool in the field of fluid mechanics. Due to recent improvements in electronics and materials, the application of hot-wire anemometry has been extended to measurement of velocity, turbulence, temperature, and mass flow in both liquids and gases. One area of interest is the study of flow properties at high temperatures and pressures. The shock tube is ideally suited to produce these conditions. In order to take valid experimental data the researcher must have complete working knowledge of this data taking equipment and its limitations. The field of hot-wire anemometry in the past has primarily concerned itself with quasi steady-state flows where the hot-wire can be calibrated at nearly the same flow conditions as its intended use. In the rapidly changing state which takes place in a shock tube, however, the problems of calibration becomes more demanding. There is not time for the wire supports to come up to the gas temperature and stabilize prior to taking data as is the case during calibration. Rather, there are usually less than ten milliseconds of data taking time under shock tube conditions when attempting to measure flow conditions

Abstract

This investigation explored the suitability of the TSI IFA-100 Intelligent Flow Analyzer system, with TSI 1210 and 1214-T1.5 hot-wire sensors, to measure the velocity behind the incident shock wave in a shock tube. Additionally, velocity fluctuations as a result of Kármán vortex street formation behind a 3/16-inch cylinder were also measured. The range of Reynolds numbers was $23,000 < Re < 35,000$ in this configuration.

Calibration of the hot-wire was accomplished from ambient temperature to 275° F with individual calibrations at discrete temperatures (ie. 74° F, 175° F, 275° F) designed to cover the expected test conditions up to 200° F and 620 ft/s. Velocities measured ranged from 312 to 590 ft/s with 4 percent or better accuracy. Velocity fluctuations were measured and computed as turbulence intensities, and ranged from 1.75 to 9.52 percent.

The results of the investigation showed favorable indication that velocity can be measured with reasonable accuracy in a shock tube with the IFA-100 system.

\bar{u}	average time variant velocity, ft/s
V	average velocity, ft/s
V _{2calc}	calculated actual velocity, ft/s
V _{2HW}	velocity measured by the hot-wire, ft/s
V _{sub}	velocity corresponding to M _{sub} , ft/s
V.T.S.	variable time setting for oscilloscope, s/div
V.V.S	variable voltage setting for oscilloscope, v/div
ω	fundamental frequency, Hertz
W _{sp}	specific weight, lbf/cu ft
W _s	shock wave speed, ft/s
X	pressure transducer output voltage, volts
*	"collapsed-linear" designator
**	"interpolated" designator

M_s	shock wave Mach number
M_{sub}	subsonic Mach number downstream of shock
n	Reynolds number exponent (same as RXP)
ν	kinematic viscosity, ft^2/s
Nu	Nusselt number
P	power, Btu/s
P_2	static pressure in region 2, psia
P_{baro}	barometric pressure, psia
Pr	Prandtl number
$PRXP$	Prandtl number exponent modifying the intercept
$PRX2$	Prandtl number exponent modifying the slope
ρ	density, lbm/cu ft
R	universal gas constant, 53.34 ft-lbf/lbm-°R
Re	Reynolds number
RXP	Reynolds number exponent (same as n)
R_c	cold probe resistance, ohm
R_h	operating or hot resistance, ohm
R_w	wire resistance, ohm
R_b	resistance at boiling point, ohm
R_i	resistance at ice point, ohm
R_f	resistance at fluid temperature, ohm
R_r	reference resistance, ohm
S	Strouhal number
T_w	operating temperature of wire, deg
T_c	cold or ambient temperature, deg
T_f	fluid temperature, deg
T_m	mean temperature, deg

List of Symbols

<u>Symbol</u>	<u>Description</u>
α	temperature coefficient of resistance, /deg
A	intercept of calibration curve
B	slope of calibration curve
C	speed of sound, ft/s
C _p	specific heat at constant pressure, Btu/lbm-°R
d	hot-wire diameter, ft
DELTA	percent error based on reading of actual vs. measured velocity
E	modulus of elasticity, KSI
E _s	anemometer output voltage (DC), volts
E _{ac}	anemometer output voltage (AC), volts
f	frequency, Hertz
F	non-dimensional frequency
γ	ratio of specific heats
g	gravitational acceleration, ft/s
g _c	universal gravitational constant, (32.174 lbm-ft/lbf-s ²)
H _f	heat transfer per unit length, Btu/hr-ft
I(x)	moment of inertia, ft ⁴
I	current, amps
K	thermal conductivity, Btu/hr-ft
L	length of hot-wire, ft
μ	viscosity, lbm/ft-hr
M	Mach number

List of Tables

<u>Table</u>		<u>Page</u>
I	Test instrumentation	83
II	Measured and derived voltage, temperature, and pressure data used to determine velocity of air behind incident shock wave	91
III	Actual versus measured air velocity behind incident shock wave	93
IV	Measured and derived data including Mach, Reynolds, Nusselt, and Prandtl numbers for the conditions behind the incident shock wave	95
V	Turbulence intensity as a function of air velocity behind the incident shock wave . . .	97

45. Photograph of an Oscilloscope Trace Showing Mechanical Vibration Superimposed on a Hot-Film Signal	78
46. Schematic of Instrumentation and Support Equipment	94
47. Truncated Cone Used to Model Hot-Film Mechanical Vibration	96

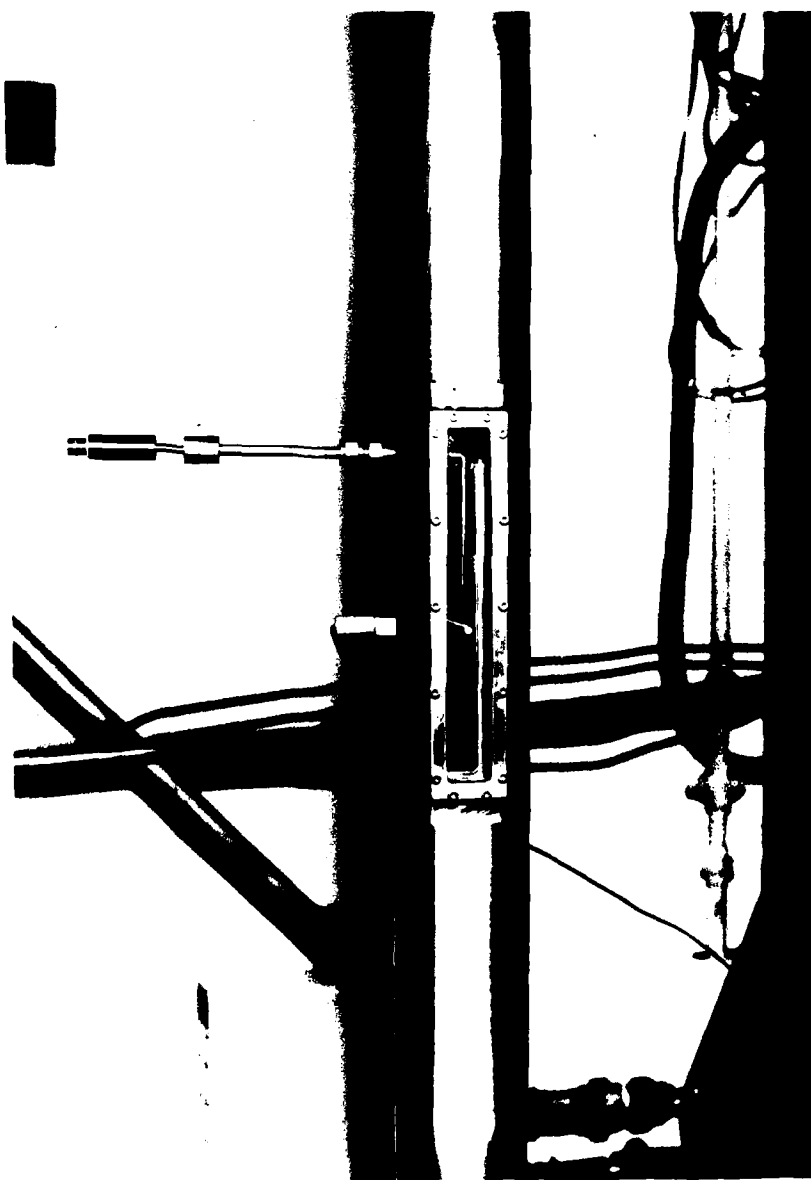


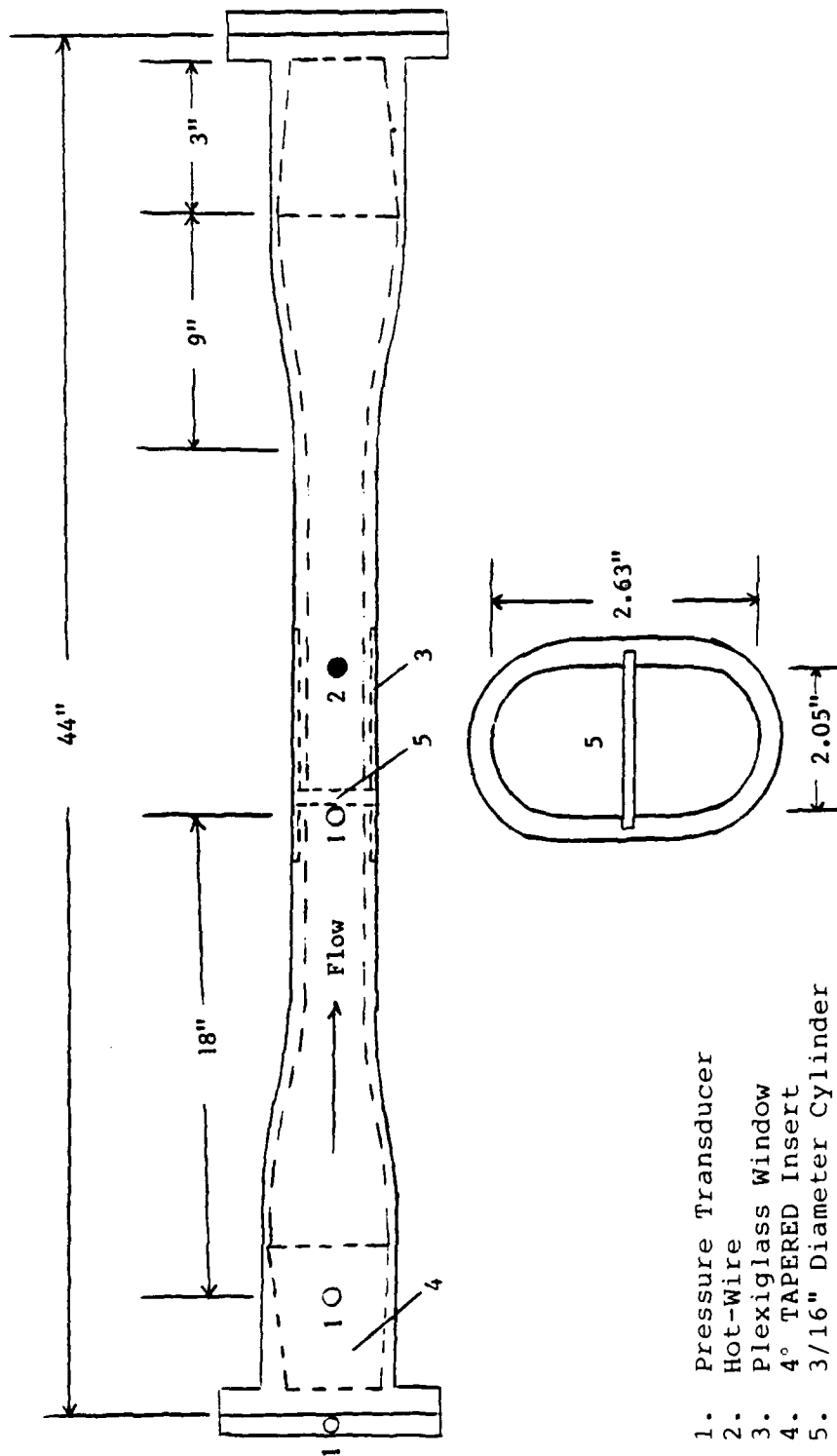
Fig 3. Test Section Showing Proximity
of Hot-Wire Probe to the Cylinder.

the desired test condition. The particular diaphragm used must be able to withstand this pressure (determined experimentally, ref. 4). The double diaphragm center region is then isolated by closing a valve, and the driver section is further pressurized to the desired operating pressure. Diaphragm rupture is controlled by evacuating the center diaphragm region to ambient conditions external to the shock tube. This causes a high pressure differential between the high pressure driver section and the upstream diaphragm inducing rupture in the upstream diaphragm first and the downstream diaphragm second. Diaphragms used included .001 and .002 inch thick Mylar specially cut to fit the double diaphragm jig. The one-mil diaphragms burst at approximately 45 psia which effectively allowed testing from 45 to 70 psia when used in the double diaphragm mode. The two-mil diaphragms burst at approximately 85 psia with a double diaphragm testing range from 85 to 150 psia. These correspond to a shock Mach number range of $1.313 < M < 1.436$ for the .001-inch thick Mylar, and $1.492 < M < 1.664$ for the .002-inch thick Mylar.

Test Section. The test section (figure 3) was made from circular, 3-inch outside diameter, 1/4-inch thick stainless steel tubing. The tubing was machine-pressed to a 2.05-inch inside width at the narrowest point. Pressing was done to facilitate a flat surface for two

8-inch long, 1-inch wide, 1/2-inch thick plexiglass windows for visual access to the test section, necessary for hot-wire probe orientation to the gas flow. Stainless steel inserts were pressed under high pressure into the tubing with a 4° taper to allow smooth transition and prevent secondary shocks from forming due to inner-wall shock tube/test section mismatch in diameters. The overall test section was 44 inches long with pressure transducers for measuring shock wave speed located 18-inches apart, as shown in figure 4. The pressure transducers served to measure test section pressures (P1, P2), trigger counters used to measure shock wave speed (W_s), to trigger an oscilloscope to photograph pressure traces, and to trigger the transient response recorder used to capture and store the hot-wire anemometer signal. A port for the hot-wire probe support was located in a position to a) center the hot-wire in the plexiglass window to verify its orientation with respect to the gas flow, b) be collocated with the downstream pressure transducer so that all test flow conditions were measured at the same location, and c) provide easy access for installation of the hot-wire probe through the window.

Air Supply. Dry, compressed air was used throughout testing to reduce the probability of hot-wire probe breakage due to unfiltered air. Control of the bottled air was via solenoid actuated valves operated from a centralized control panel.



1. Pressure Transducer
2. Hot-Wire
3. Plexiglass Window
4. 4° TAPERED INSERT
5. 3/16" Diameter Cylinder

Fig 4. Schematic of Test Section Showing Hot-Wire Probe and Transducer Locations.

III. Theory of Hot-Wire Operation and Calibration

Theory of Operation

The hot-wire anemometer is a device which uses a probe with a very thin metal wire, often made of Platinum-iridium or Tungsten, which when heated by an electric current follows a linear temperature-resistance relationship shown in equation (1),

$$R_W = R_R[1 + \alpha(T_W - T_R)] \quad (1)$$

King (5) first established that the heat transfer rate dH/dt is given by,

$$dH/dt = (A + B \sqrt{\rho} v) (T_W - T_f) = P = I^2 R_W \quad (2)$$

Since then, the field of anemometry has progressed to its current state employing advanced electronics, the most popular type being the constant temperature anemometer. It is so coined because it employs a feedback circuit within a wheatstone bridge controlled by an amplifier which adjusts current flow to maintain constant wire resistance and hence constant temperature. According to many sources including Bradshaw (6), electrical power applied to the wire is transferred away from the wire by radiation, bouyant convection, conduction along the wire to its end supports, and through forced convection by the

fluid flow. Radiation (about 0.1% of electrical output) and bouyant convection for flows above 5 cm/s, can be neglected. Hence, wire conduction and forced convection to the fluid flow make up the greatest losses and account for the bulk of the heat transfer adjustments to the calibration assumptions. Reference (7) gives many useful sources which comprise the bulk of the field of hot-wire anemometry to date, and can serve as a historical guide. An expression for a hot-wire calibration, taken from Bradshaw (6), can be written,

$$\frac{H_f}{T_w - T_f} \propto \frac{I^2 R}{R_w - R_f} = A(T_f) + BV^n \quad (3)$$

The combination relating resistance to heat transfer in equation (3) can be related directly to the voltage squared (E_s^2) and can be further simplified to yield the Nusselt number shown in equation (4).

$$Nu = \frac{E_s^2 R_w}{K (R_w + R_f) L (T_w - T_f)} \quad (4)$$

Collis and Williams (8) recommend that in equation (3) $n = 0.45$ for $Re < 44$ and $n = 0.51$ for $44 < Re < 140$ where Re is the Reynolds number.

Ultimately, universal correlation of heat transfer effects is not likely due to such wide application of the

hot-wire rendering individual wire calibration necessary for each instance. In the case of a shock tube application, it was not likely at the outset of the research that conventional exponents, like the values for n proposed by Collis and Williams would suffice. Indeed, rather than follow a conventional 0.45 (Collis and Williams) or 0.5 (King) power law for the exponent, exponents used to linearize the calibration data would have to be individually determined for best results.

The calibration calculations used for this shock tube application, taken from Rivir (9), lend themselves to a form which include in its simplest form Nusselt number versus Reynolds number. These calculations are presented in Section VI.

In addition to average gas velocities behind the incident shock wave, levels of velocity fluctuation are also of interest. After replacing velocity with Reynolds number in equation (3) equations (3) and (4) can be differentiated with respect to time to give turbulence intensity, defined by Schlichting (10) as the ratio of the time varying root-mean-square velocity to the local mean velocity. Turbulence intensity is given by equation (5).

$$\frac{\sqrt{u}}{V} = \frac{2Nu}{n B Re^n} \left(\frac{E_{ac}}{E_o} \right)^2 \quad (5)$$

While turbulence is not expected in the region being investigated in the shock tube, a calculation of turbulence intensity was made, as an analogous means of determining levels of velocity fluctuation associated with the Kármán vortex street that is shed from a cylinder in cross flow.

Calibration

General. Calibration of hot-wire and hot-film sensors is conventionally performed at actual test conditions. This can be faithfully reproduced under many steady-state experimental conditions in which the prongs and support are brought to the same temperature as the flow. In shock tube investigations, however, actual test time is on the order of a few milliseconds and the prongs and supports are not brought to the same temperature as the flow behind the shock wave. Rather, they retain the temperature of the low pressure test section prior to shock passage (ie. Room temperature) (11). For this reason, a calibration of the hot-wire performed in steady-state flow is not directly applicable to measurement in a shock tube, due to the fact that the conditions of thermal conduction from the wire to the prongs cannot be easily compared in the two cases. Hence, there are inescapable errors due to this heat transfer difference from the steady flow calibrator to the shock tube environment. Additionally, the characteristic temperature and pressure rise following

shock passage requires a hot-wire calibration over a broad temperature and pressure range if the same hot-wire probe is to be used over a wide range of test conditions.

Hot-Wire Anemometer Calibrator. The calibrator used (figure 5) to produce the hot-wire calibration curves shown in section VI was fabricated by AFWAL Aero Propulsion Laboratory, Wright-Patterson AFB. It was modeled after a TSI Model 1125 Calibrator. The calibrator permits calibration over a wide range of flow temperatures. The heat source is a coil with a Variac autotransformer in line to control the current flow. The calibrator has a series of screen grids to break up the central core of airflow which passes from the inlet valve into a stilling chamber. Here the air is stagnated until it passes through a 1/8-inch nozzle. Nozzle size selection was based on the capability of the heater/Variac to heat the mass flow rate required for the temperature (275° F) and velocity range (300-900 ft/s) of interest. It was found experimentally that a larger nozzle diameter increased the mass flow beyond the heating capability of the system. Additionally, the nozzle diameter was chosen to be large enough so that the hot-wire could be fixed at the same plane as the orifice opening, ie. in the opening itself, without damaging the sensor. Total pressure and thermocouple ports were located at equal levels so stagnation temperature and pressures could be measured at

1. Probe Support
2. 1/8" Diameter Nozzel
3. Pressure Port
4. Thermocouple Port
5. Screen
6. Valve
7. Regulator
8. Filter
9. Variac-Autotrans-
former
10. Heat Source

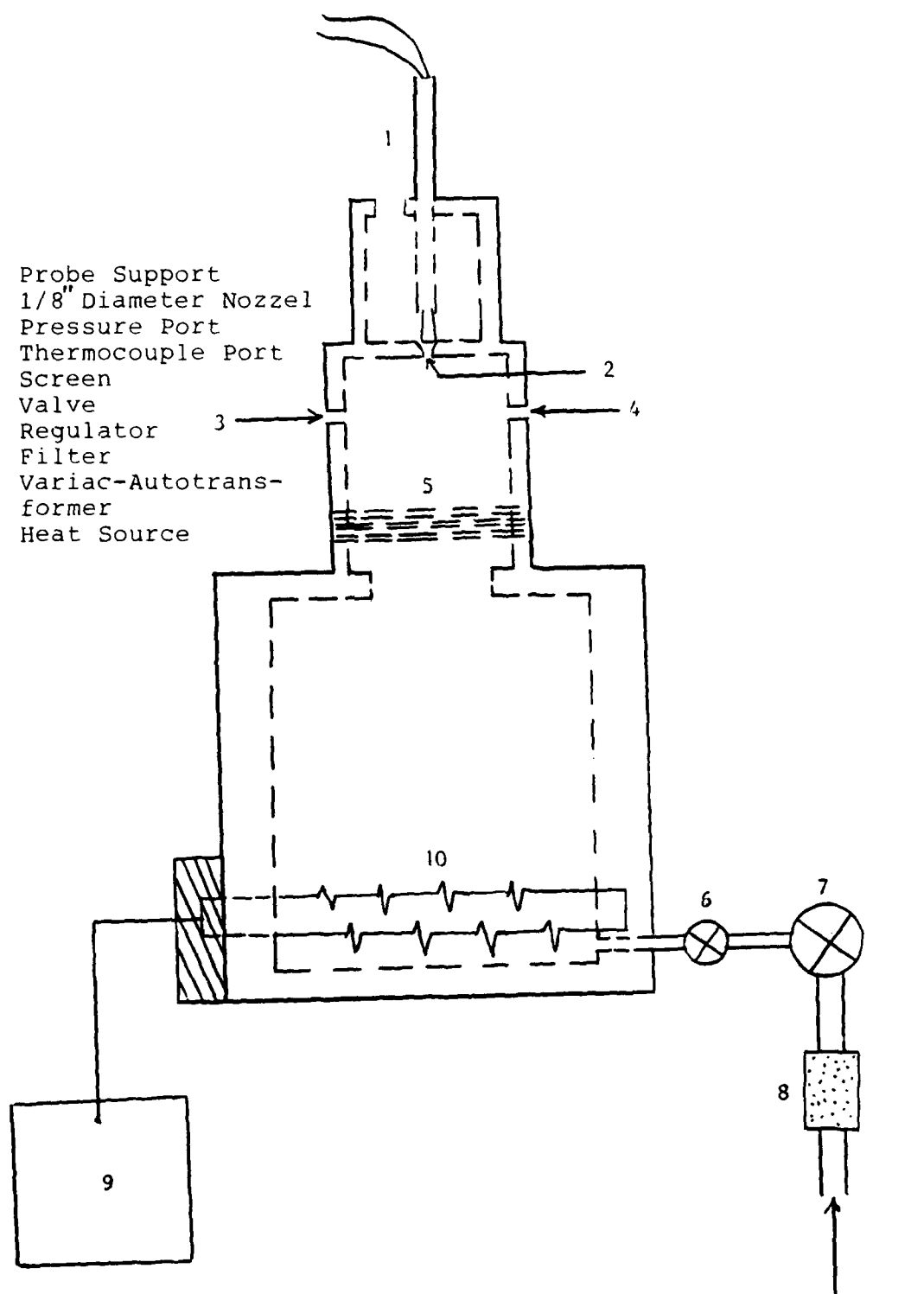


Fig 5. Schematic of Calibrator Used to Calibrate Hot-Wire Probes.

110 PSIA air

the same flow conditions. The stagnation pressure was measured with a U-tube mercury manometer and the stagnation temperature with a bare-wire copper-constantan thermocouple insulated with glass to separate the leads and reduce heat conduction from the walls of the calibrator. Thermocouple signals were input to a HP-9845B computer with existing software to reduce the thermocouple signals to temperatures. A complete listing of instrumentation used during testing is given in Appendix A.

IV. Calibration and Test Procedure

Calibration

Pressure Transducers. Calibration of all pressure transducers was performed simultaneously while installed in the shock tube using a previously calibrated Bourdon tube pressure gauge as a reference. The Bourdon tube gauge was calibrated by using a dead weight tester.

Hot-Wire Anemometer. The calibration procedure was designed to cover velocities ranging from 300-900 ft/s, and static temperatures up to 275° F. The sensors used during the calibration and subsequent testing were Thermo-Systems Inc. (TSI) 1214-T1.5 and TSI 1210-T1.5 single wire probes (.00015 in diam., Tungsten), and TSI 1214-10 film sensors (.001 in diam.). The recommended operating temperature for the T1.5 probe is 250° C, but it was found that probe sensitivity decreased dramatically as the air temperature approached the wire temperature, held constant by the TSI Model 150 anemometer. Maximum T1.5 probe temperature listed by TSI is 300° C. It was first determined to operate the wire at 290° C to increase sensitivity to the flow conditions, but remain within the structural constraints of the wire, however voltage/velocity sensitivity was so low as to render operation at this wire temperature impractical. The wire temperature was increased beyond recommended structural limits to

316° C in order to achieve suitable sensitivity. This was accomplished with limited success as several wires were destroyed during calibration while full range sensitivity spanned only 0.2 volts from 0-900 ft/s gas velocities. A lack of higher temperature-capable hot-wires precluded further gains in sensitivity. The 1214-10 film sensor has a maximum recommended operating temperature of 300° C, however further calibration and testing of hot-film probes was dismissed due to a resonant vibration which induced voltages far in excess of those induced by air passage following the shock wave. (Discussed in Appendix B)

The overheat setting used during calibration was determined as follows,

$$R_h = (R_b - R_i)/100 (T_w - T_c) + R_c \quad (6)$$

where R_b and R_i are wire resistance at the boiling and ice points, respectively.

$$\text{OVERHEAT} = R_h/R_c \quad (7)$$

Once the wire cold resistance (R_c) was determined, the operating resistance (R_h) was calculated and input to the anemometer.

The laboratory air supply was passed through a filter to remove potential wire damaging particles and through a pressure regulator to maintain constant pressure at the calibrator inlet valve (figure 5). Compressor and regulator pressure were held constant above the pressure required to choke the flow at the calibrator inlet valve to assure constant mass flow throughout the calibration. This was necessary since all testing was performed where compressibility effects must be accounted for. The calibration method prescribed by Norman (12) accounts for compressibility and constant mass flow by plotting anemometer output (voltage) versus ρV , but does so at only one temperature. Shock tube applications require a span of temperatures, so three calibrations were performed at ambient, 175° F, and 275° F to cover the range of test temperatures.

Measurement Procedures

Measurement procedures were accomplished as follows after all equipment was warmed up thoroughly. Hot-Wire Anemometer - Null the bridge and determine "cold" resistance of the probe. Set overheat ratio to the same overheat ratio used during probe calibration, thereby setting the "hot" or operating resistance of the probe. Verify position and alignment (90° to flow) of the hot-wire probe by examining through the test section

VI. Discussion of Results

The purpose of this research was to investigate the suitability of the IFA-100 Intelligent Flow Analyzer with the TSI Model 150 anemometer to measure velocity and levels of velocity fluctuation behind the incident shock wave in a shock tube. Since the results expected would cover a wide range of temperatures and pressures, a technique was developed to calibrate the hot-wire anemometer over the expected data range.

Calibration

Calibration was successfully performed for one TSI 1214-T1.5 and one TSI 1210-T1.5 hot-wire probe, the first hereafter referred to as K481 and the second referred to as B052. The first few calibration attempts proved futile as sensitivity to velocity was so low above 300 fps it fell outside the limit of the capability of the anemometer to record voltages with any certainty for the velocities anticipated in the shock tube. This was attributed to a relatively small difference between the temperature of the air flowing past the wire during calibration and the temperature of the hot-wire itself. As the two temperatures approach one another, sensitivity to velocity decreases because the relatively small temperature gradient from the wire and its supports to the fluid which

The root-mean-square value of the time varying voltage component, E_{ac} , was found by applying equation (19).

$$E_{ac} = \sqrt{\sum_{i=1}^j \frac{(E_{ac} - E_o)^2}{j}} \quad (19)$$

Although true turbulence was not present in the region tested, a measure of velocity fluctuation is roughly analogous to turbulence intensity. Turbulence intensity is found by applying equation (5).

$$\frac{\sqrt{\bar{u}^2}}{V_{2HW}} = \frac{2 Nu}{n B Re^n} \left(\frac{E_{ac}}{E_o} \right)^2 \quad (5)$$

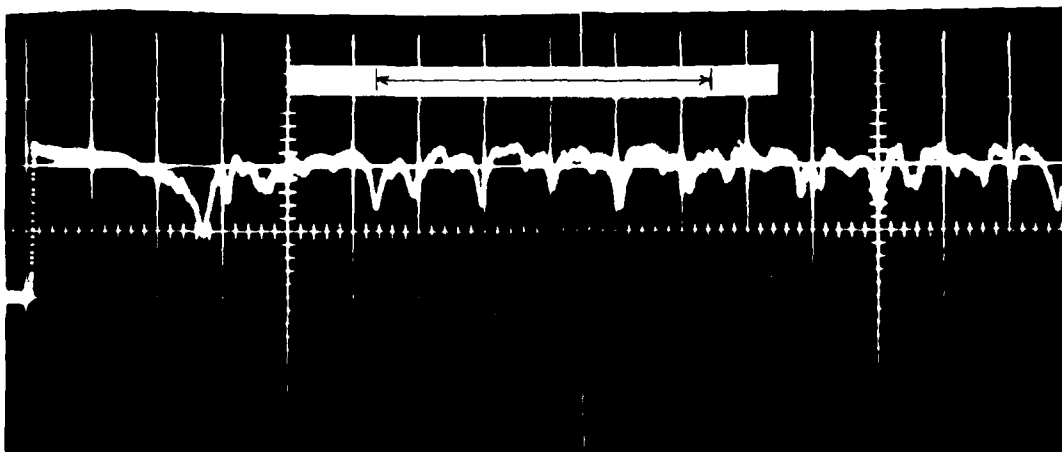


Fig 13. Photograph of an Oscilloscope Trace Showing the Anemometer Signal Captured by a Transient Response Recorder.

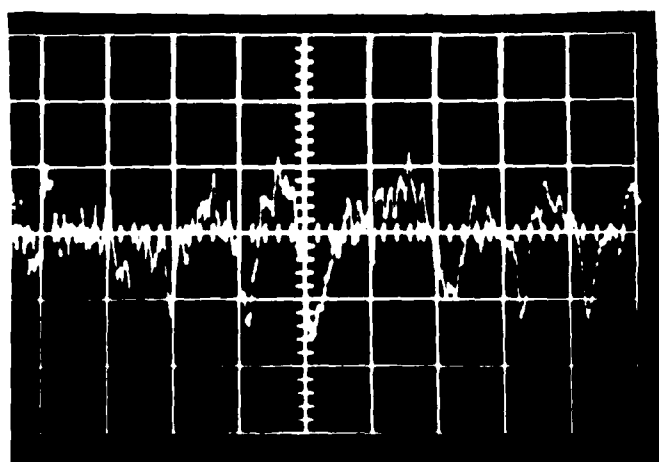


Fig 14. Photograph of an Oscilloscope Trace Showing Increased Voltage Sensitivity.

the system stabilize to give a nominal output. Unfortunately, considerable delay must be set within the oscilloscope to record a sufficient amount of anemometer signal to be able to discern true velocity fluctuation from electronic overshoot, damping, etc. This delay time also changes with each new test condition making all measurements a trial and error procedure. A Transient Response Recorder was used to capture more of the signal to determine the point in the trace that electronic transients end and true velocity perturbations begin. Figure 13 shows a photograph of the anemometer signal as captured by the Transient Response Recorder and output to an oscilloscope. For purposes of data reduction, the only portion of the signal used to record velocity fluctuation was that taken from the Transient Response Recorder and is indicated by the region between the arrows in figure 13. Additionally, the voltage sensitivity on the oscilloscope was increased (after the signal was captured) in order to more accurately measure levels of velocity fluctuation. The amplified signal is shown in figure 14.

All transient velocity data was digitized similarly to the procedure used for pressure and average velocity signals by using an HP-9874A digitizer and HP-85 computer. The nominal number of readings (digitized) per cycle was 10-12 for approximately 10 cycles (indicated by the arrows in figure 13) for all data taken.

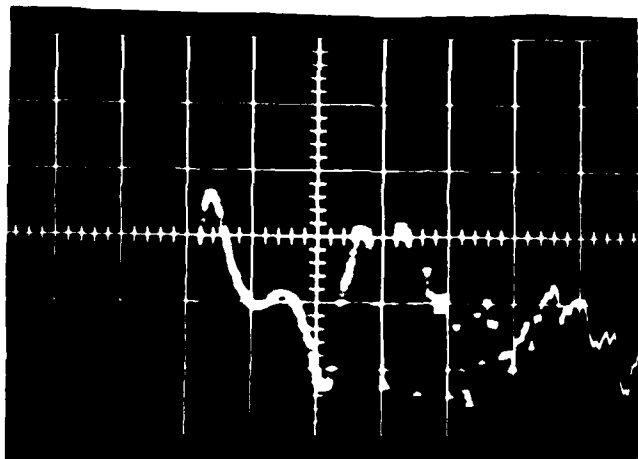


Fig 12a.

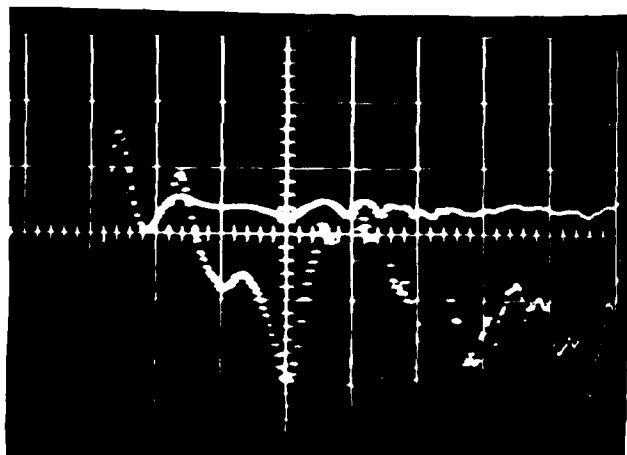


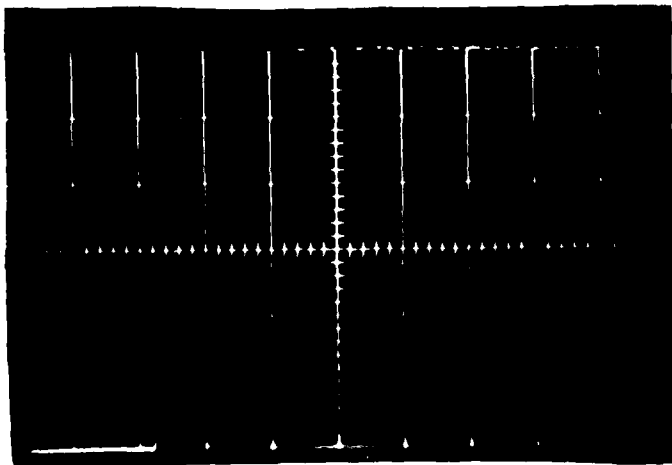
Fig 12b.

Fig 12. Photographs of Oscilloscope Traces
Showing the Initial Part of the Hot-Wire Signal
as the Shock Wave Passes the Probe.

Kármán Vortex Streets

A TSI 1210-T1.5 hot-wire probe placed at a location 4 diameters behind a 3/16-inch circular cylinder measured levels of velocity fluctuation associated with Kármán vortex street (15) formation. Turbulence is defined as "three-dimensional time-dependent motion in which vortex stretching causes velocity fluctuations to spread to all wavelengths between a minimum determined by viscous forces and a maximum determined by the boundary conditions of the flow ... and randomness is the essential characteristic.." (6). True random turbulence was not expected in the region behind the cylinder in the shock tube where the hot-wire probe was placed. Figure 12 presents two independent test runs showing the initial part of the hot-wire signal just as the shock wave passes the probe. Both traces were output directly from the anemometer to the oscilloscope. It should be noted that both traces, with initial driver pressures (P4) of approximately 55 psia are nearly identical, that is they very nearly follow the same time history. The two traces in figure 12b are identical except that each was photographed at a different voltage sensitivity.

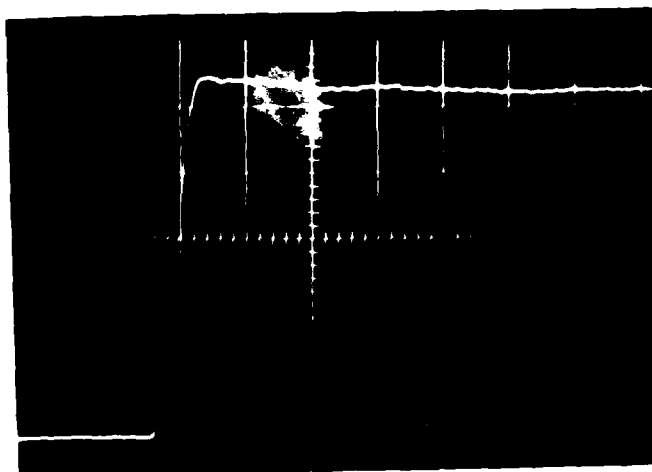
Since randomness is an inherent feature of turbulence, it is surmised that this initial portion of the signal consists of initial rise (after shock passage), an overshoot, and a damping period before the electronics of



$E_s = 2.087$ volts

$V2 = 618.5$ ft/s

Fig 10. Photograph of an Oscilloscope Trace Showing Anemometer Output for the Highest Velocity Tested.



$E_s = 1.893$ volts

$V2 = 325.3$ ft/s

Fig 11. Photograph of an Oscilloscope Trace Showing Anemometer Output for the Lowest Velocity Tested.

Transient Response Recorder and output to an oscilloscope for photographing. The trace was interpreted by digitizing the signal as was done previously for the pressure data, and arithmetically averaged to obtain a DC voltage corresponding to the average velocity of the air in region 2. Figure 9 shows a comparison of signals when (1) the anemometer signal was output directly to an oscilloscope (figure 9a), and (2) when the anemometer signal was input to the Transient Response Recorder before output to the oscilloscope (figure 9b). Note that the drop off in figure 9b is not a physical occurrence but rather a characteristic of the Transient Response Recorder to repeat a stored signal.

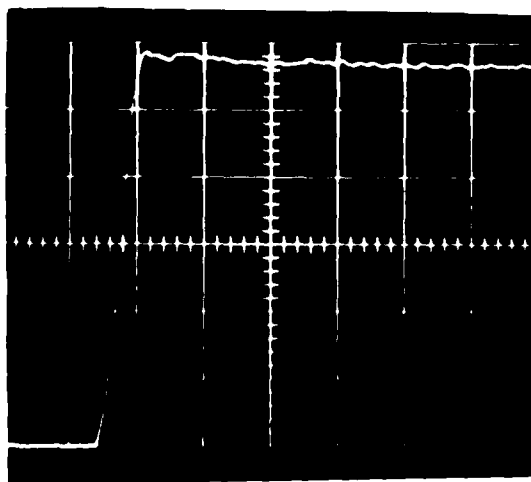


Fig 9a.

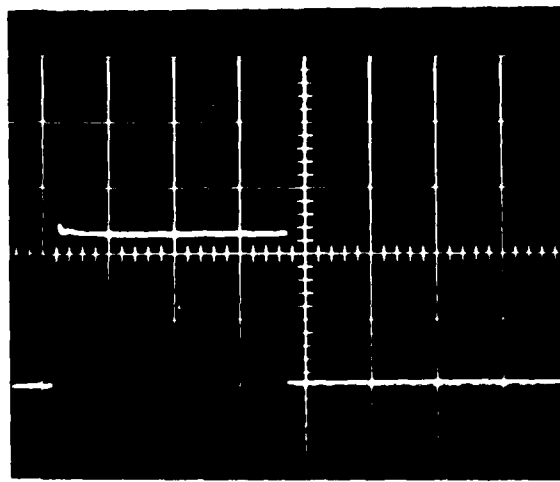


Fig 9b.

Fig 9. Photographs of Anemometer Output Signals Showing (9a) Output Directly to an Oscilloscope, and (9b) Input to a Transient Response Recorder Before Output to an Oscilloscope.

The actual velocity (the velocity deemed to be the true velocity) of the gas in region 2 will hereafter be referred to as V_{2calc} . This was the velocity that the velocity measured by the hot-wire was compared against to determine accuracy.

$$W_S = ds/dt \quad (12)$$

$$C1 = \sqrt{g_C RT1} \quad (13)$$

$$M_S = W_S/C1 \quad (14)$$

$$M_{sub} = \left[\frac{M_S^2 + \left(\frac{2}{\gamma + 1} \right)}{\left(\frac{2\gamma}{\gamma + 1} \right) M_S^2 - 1} \right]^{1/2} \quad (15)$$

$$C2 = \sqrt{g_C RT2} \quad (16)$$

$$V_{sub} = M_{sub} C2 \quad (17)$$

and,

$$V_{2calc} = W_S - V_{sub} \quad (18)$$

Hot-wire signal data reduction was performed as follows; the hot-wire voltage output was stored on a

Equations (9) and (10) assume that the shock wave propagates into a gas at rest with respect to laboratory fixed coordinates, which is applicable to this research.

Temperature

Theoretical values of temperature in region 2, T_2 , were computed from the incident shock Mach number and initial temperature, T_1 . The following temperature relationship taken from Gaydon and Hurle (2) was used.

$$T_2/T_1 = \frac{[\gamma M^2 - (\gamma - 1)/2][((\gamma - 1)/2)(M^2) + 1]}{((\gamma + 1)/2)^2 M^2} \quad (11)$$

Equation (11) assumes that both driver and test gases are ideal, have the same ratio of specific heats, and the same speed of sound (when at the same temperature, ref. 2).

Air Velocity

The velocity of the air in region 2, V_2 , once the shock had passed, was determined by using initial conditions and wave speed in a shock-fixed coordinate system. Normal-shock relationships (13) were applied to determine the Mach number of the flow conditions in region 2. The air velocity behind the incident shock was found in laboratory-fixed coordinates through transformation. The following equations were used to determine the calculated velocity in region 2, referred to as V_{2calc} .

The change in voltage is a measure of gauge pressure and was determined by using an HP-9874A digitizer and HP-85 computer. The pressure, P_2 , was then computed from the following relationship,

$$P_2 = P_{\text{baro}} + A + BX \quad (8)$$

where

P is the pressure sought

P_{baro} is barometric pressure

X is the voltage output of the pressure transducer

and

A & B are the intercept and slope for the linear calibration curve of the pressure transducer

Measured values of pressure are compared with the theoretical shock tube equations (2) for static pressure change given by,

$$P_2/P_1 = \frac{2\gamma M^2 - (\gamma - 1)}{(\gamma + 1)} \quad (9)$$

and

$$P_4/P_1 = \frac{2\gamma M^2 - (\gamma - 1)}{(\gamma + 1)} \left\{ 1 - \frac{\gamma - 1}{\gamma + 1} (M - 1/M) \right\} - 2\gamma/(\gamma - 1) \quad (10)$$

V. Data Reduction

Shock Velocity

The speed of the incident shock wave, W_s , was determined by dividing the time taken from a counter into the distance between two pressure transducers which triggered the counter. A backup counter was used to provide insurance against loss of data. The distance between a pressure transducers was 18-inches for all data taken.

Pressure

All pressures were measured with absolute pressure transducers rated at 100 psia. Pressures in region 2 behind the shock wave were determined by adding barometric pressure (the pressure in region 1) to the change in pressure recorded photographically from an oscilloscope trace. Figure 8 presents a typical pressure trace which shows the step increase indicating shock passage.

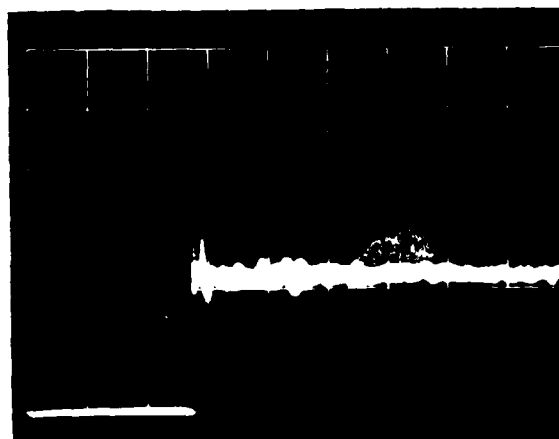


Fig 8. Photograph of an Oscilloscope Trace
Showing Pressure Rise After Shock Wave Passage.

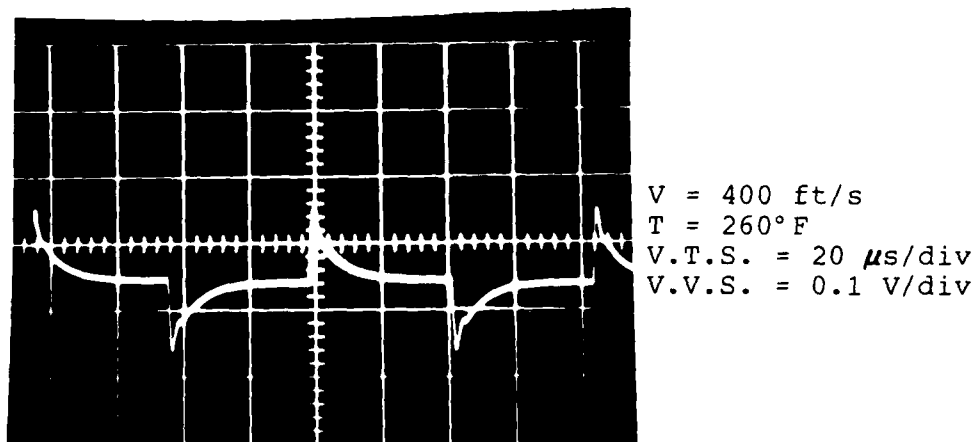


Fig 6. Photograph of an Oscilloscope Trace Showing the Frequency Response of the Hot-Wire at 400 ft/s.

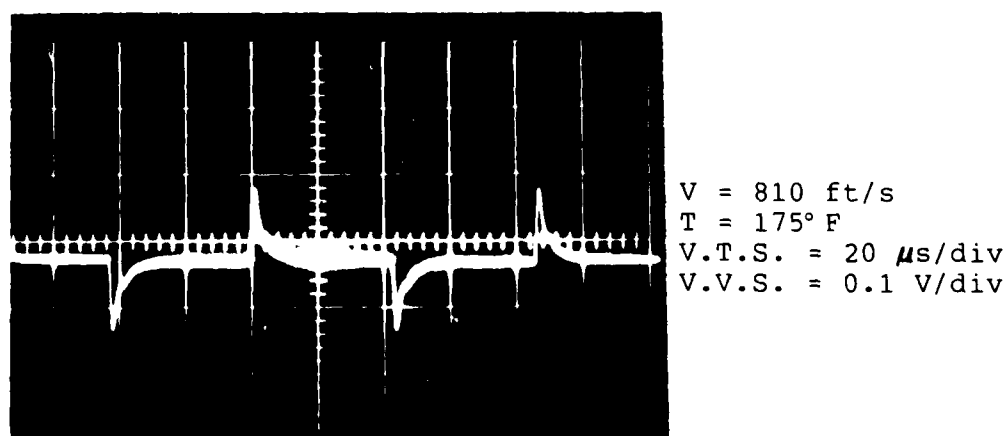


Fig 7. Photograph of an Oscilloscope Trace Showing the Frequency Response of the Hot-Wire at 810 ft/s.

window. Transient Response Recorder - Set memory to zero position and trigger switch to "arm". Shock Tube - Place diaphragm(s) in jig, insert the shock tube, and pressurize the tube to the desired pressure ratio, P_4/P_1 . Oscilloscopes - Photograph illuminated grid. Set scopes in external triggered, single sweep mode. Open shutters on cameras. Counters - Set to zero.

Fire the shock tube by evacuating the diaphragm center region. Record P_2 , W_s via counter readings, and the anemometer signal on both the Transient Response Recorder and oscilloscope photographic trace. Develop the pictures and proceed with next run.

Frequency Response

Frequency response characteristics were determined prior to each calibration by applying a square wave test as standard procedure. This was done to assure that the IFA-100 system would respond satisfactorially at the high velocities and temperatures expected during the calibration. Figures 6 and 7 show the response at the indicated test conditions. Note from the photographs that no degradation in response is apparent.

inhibits heat conduction from the wire and forced convection to the fluid. It is this heat transfer which draws more power from the anemometer system and induces the system to supply more current to hold the wire resistance (and hence temperature) constant. The current change gives rise to the voltage change being measured. TSI recommends a wire operating temperature of 250°C for the T1.5 probe. In order to increase the sensitivity of the system, the wire temperature was increased until sufficient sensitivity was achieved throughout the temperature and velocity range required. The maximum operating temperature listed by TSI for the T1.5 wire is 300° C, but this too gave marginal results for the more than 400 ft/s minimum velocities required. The final configuration yielded a wire temperature of 316°C for K481 and 300° C for B052. This yielded only marginally acceptable sensitivities and created catastrophic calibration problems as far as exceeding the structural and thermal limitations of the wire. One calibration was attempted at 325°C wire temperature but ended up with the wire breaking. Two attempted calibrations at 322°C with two separate wires also ended with the wires breaking. Calibrations were attempted with two wires, both at 316°C and one of the wires survived while the other broke. Two additional wires survived calibrations at 291°C and 300°C but yielded poor and marginal sensitivity to velocity,

respectively. No higher temperature capable wires were available which limited use of calibrated wires to K481 to (316° C) and B052 (300° C) as they remained the only hot-wire probes even marginally suitable for testing in the shock tube. Full-range sensitivity spanned approximately 0.2 volts from 0-900 ft/s gas velocities.

Final calibration reduction was achieved using a software program developed by Dr. Richard Rivir (9) of the Aero Propulsion Laboratories, Wright-Patterson AFB, Ohio, and modified to include compressibility effects and variable specific heats for air at the high temperatures encountered in the shock tube. Voltage, temperature, and pressure measured during calibration are input to the program which calculates the wire temperature as a function of fluid (air) temperature and wire characteristics (temperature coefficient of resistance). A mean temperature was calculated from the following equation,

$$T_m = (T_f + T_w)/2 \quad (20)$$

as proposed by Collis and Williams (8). The following fluid properties were evaluated: Nusselt number (equation 2), velocity (equation 21),

$$V = \sqrt{2C_p T_f [1 - (P_1/P_2)^{\gamma-1/\gamma}]} \quad (21)$$

and Reynolds number (equation 22),

$$Re = \frac{\rho V d}{\mu} \quad (22)$$

where

$$\rho = \rho (T_m)$$

$$V = V (T_f)$$

and

$$\mu = \mu (T_m)$$

Collis and Williams propose a temperature loading factor shown below, to be applied to the Nusselt number.

$$\text{LOAD FACTOR} = (T_m/T_f)^{TREX} \quad (23)$$

where $TREX$ is an exponent determined experimentally according to the wire characteristics and fluid temperature range over which the calibration takes place.

The general calibration equation, taken from Corrsin (16), and modified by Rivir (9), is given in equation (24),

$$Nu(T_m/T_f)^{TREX} = A Pr^{PRXP} + B Pr^{PRX2} Re^{RXP} \quad (24)$$

where

A = intercept

B = slope

PR = Prandtl number

PRXP = Prandtl number exponent modifying the
intercept

PRX2 = Prandtl number exponent modifying the slope

RXP = Reynolds number exponent

Collis and Williams suggest using $PRXP = 0.2$ and $PRX2 = 0.9$ for Reynolds numbers less than 140, and this was adopted for probe K481. The two Prandtl number exponents seem only to serve as scaling factors and were used primarily to expand the plotted data to the most useful scale. This can be shown in figures 15 and 16. It can be shown by extrapolation from these figures that the slope and intercept remain constant, and accuracy as determined by deviation from linearity is not compromised. The Reynolds number exponent, RXP, varies with Re , according to Collis and Williams (note that n first used in equation 3 is identical to RXP). They suggest that $RXP = 0.45$ for $0.02 < Re < 44$ and $RXP = 0.51$ for $44 < Re < 140$. Results of calibrations of K481 and B052 yield $RXP = 0.49$ and 0.46 respectively to give the "best fit" (ie. smallest deviation from linearity). The large range of temperatures encompassing the calibration make the ability to accurately match Collis and Williams results prohibitive. However, the accuracy of the velocity measured with respect to actual velocity over the entire range using Reynolds number exponents from $0.45 < RXP < 0.51$ did not vary more than 2% for any value of RXP selected within this range. Actual values chosen are

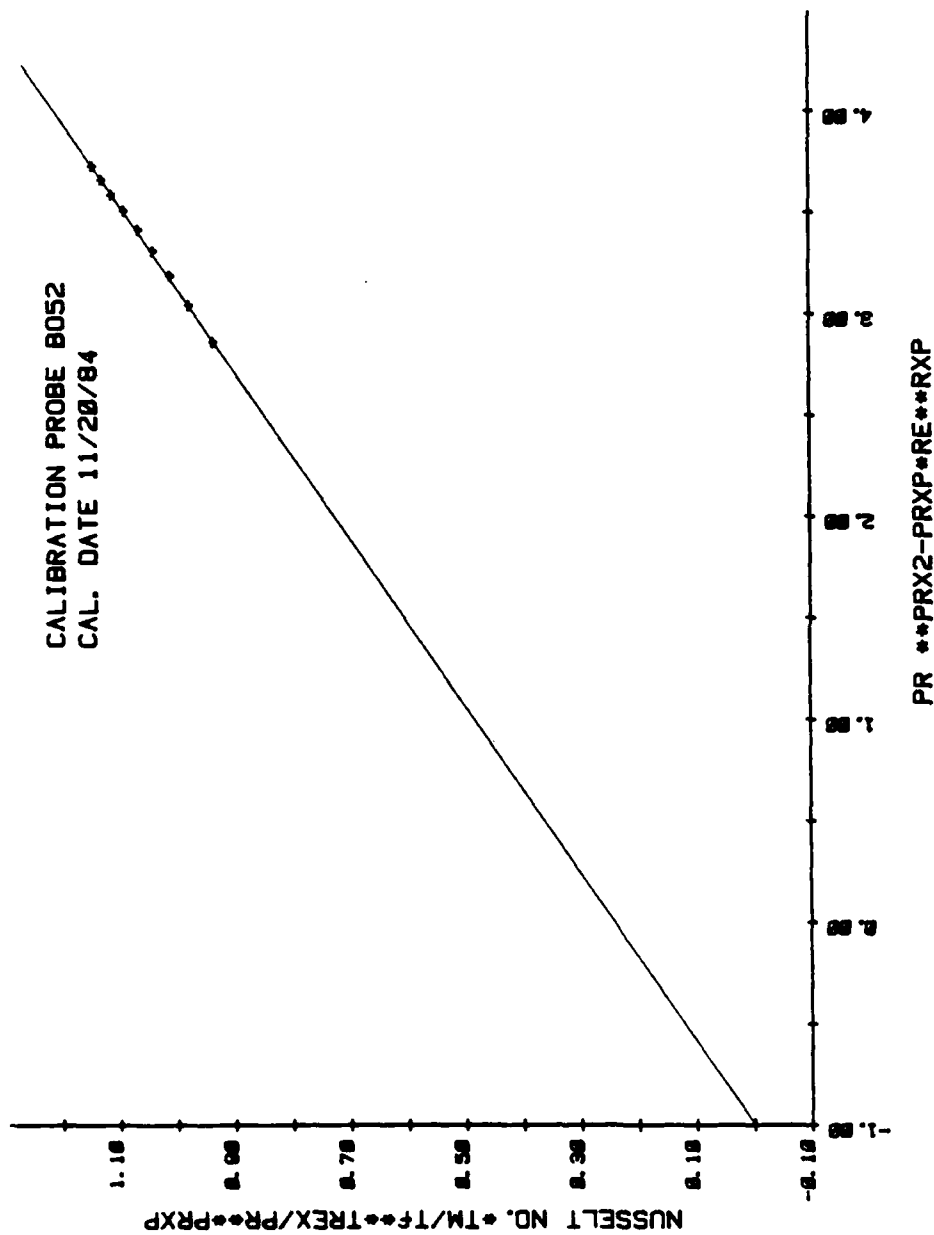


Fig 15. Calibration Plot for Probe B052 Showing Effect of Prandtl No. Exponents on 61°F Temperature Curve.
(TREX = -2.7, RXP = 0.45, PRXP = 1, PRX2 = 1)

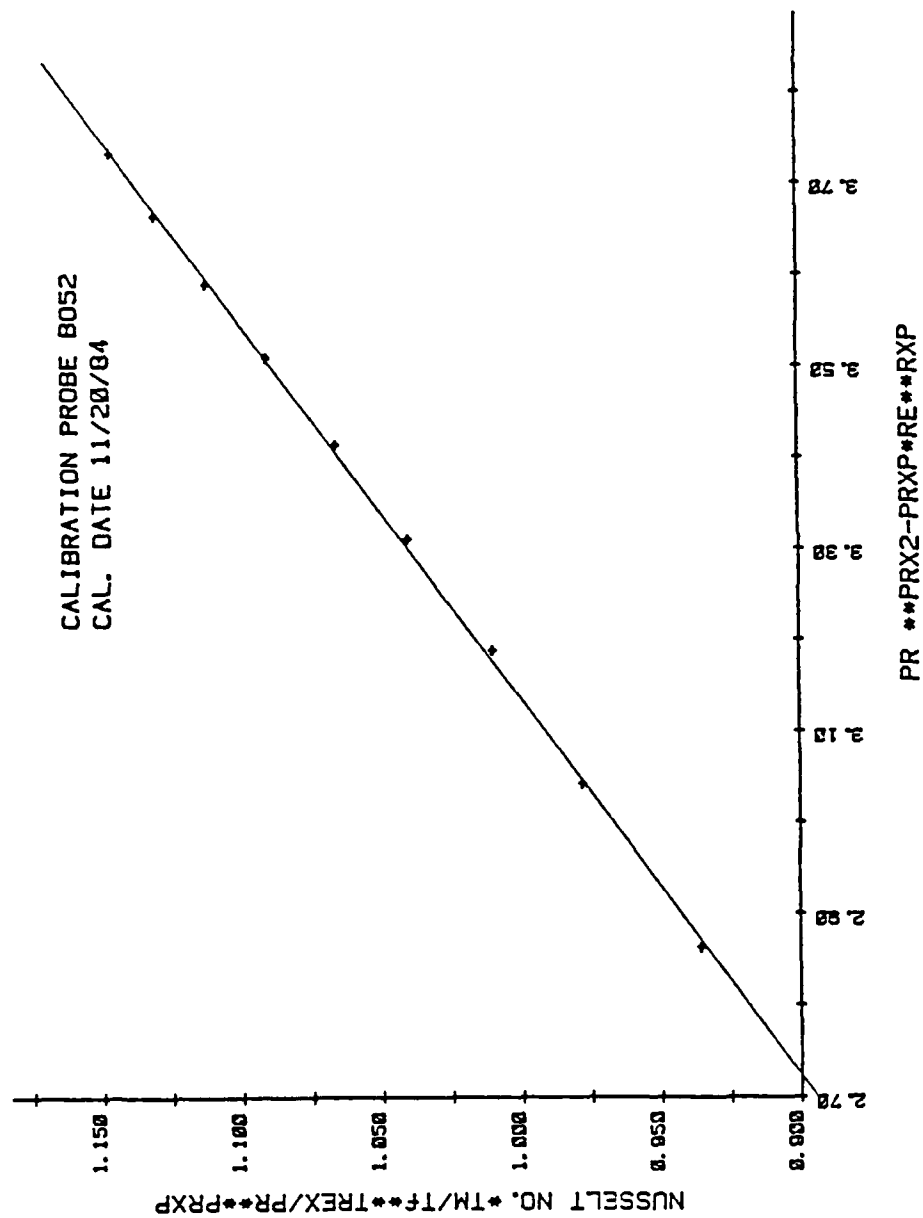


Fig 16. Calibration Plot for Probe B052 Showing Effect of Prandtl No. Exponents on 61° F Temperature Curve.
(TREX = -2.7, RXP = 0.46, PRXP = 0.9, PRX2 = 0.2)

specifically matched to the individual wire over its calibration range. Data for each probe are given in Appendix A.

Temperature loading effects appear as the fluid temperature changes. Probe K481 was calibrated over a full range of velocities at three different temperatures, 74° F, 175° F, and 275° F, the temperature range to be investigated in the shock tube. Ideally, this would give three distinct linear calibration curves with identical slopes and different intercepts which increase with temperature as shown in figure 17. With the proper temperature loading factor applied, the curves should collapse to a single linear set of data spanning the entire range of temperatures and velocities of the calibration. The temperature loading factor and Prandtl number exponents (T_{REX}, P_{RXP}, P_{RX2}) are essentially arbitrary to the extent that enough discernible interpolated temperature curves can be inserted to fulfill the task of velocity determination over the desired range. Improper exponents can cause data lumping, as in figure 15, or a collapsing of temperature curves too closely spaced to insert enough interpolated temperature curves to accurately determine velocity. Depending on the temperature loading factor exponent (T_{REX}) selected, a "crossover" of temperature curves can occur, as shown in figures 18, 19, and 20. In fact, the temperature

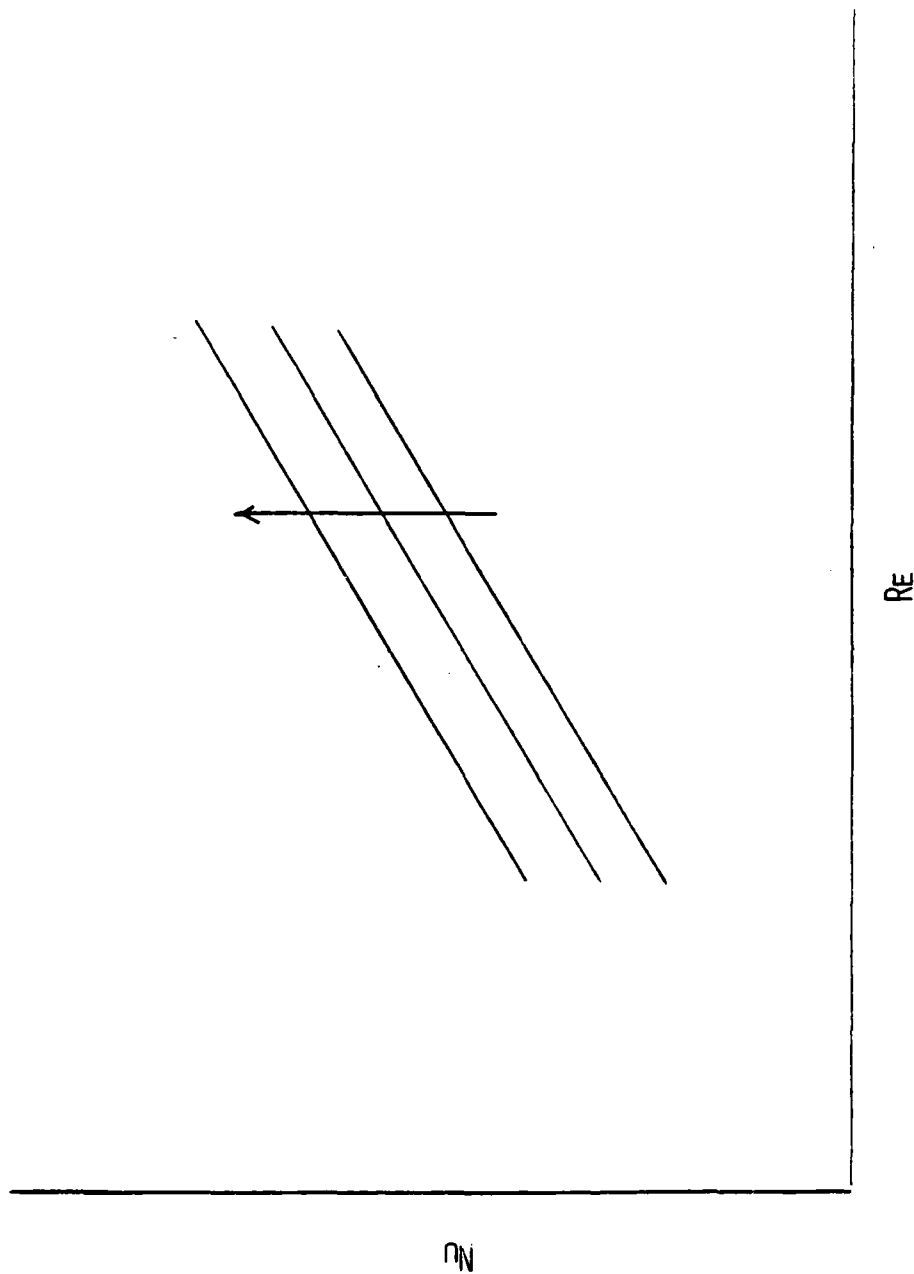


Fig 17. Ideal Variation of Nusselt No. (E_2) with Reynolds No. (Velocity) as Temperature Changes.

CALIBRATION PROBE K481
CAL. DATE 10/22/84

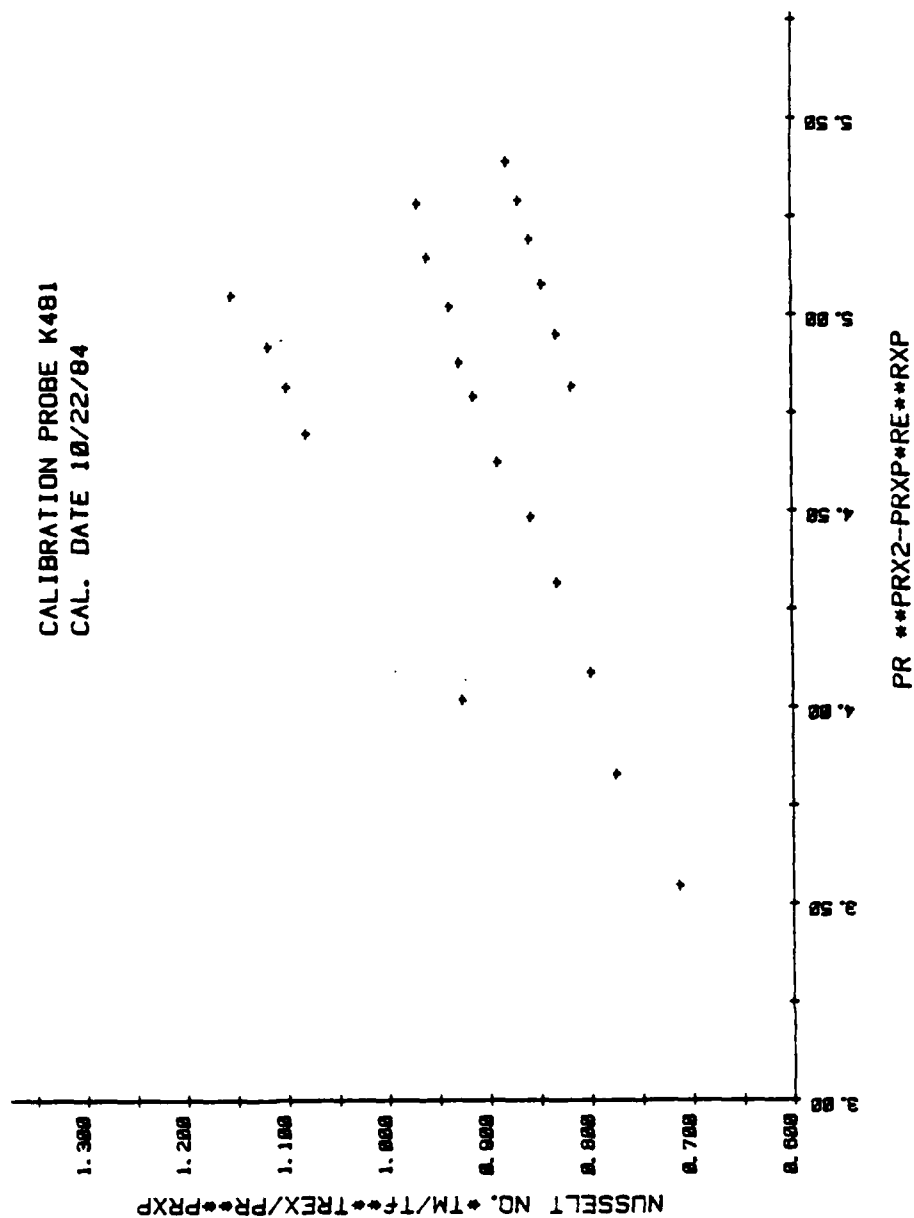


Fig 18. Hot-Wire Calibration Plot for Probe K481 Showing
74°F, 175°F, and 275°F Temperature Ranges.
(T_{REX} = -4.0, R_{XP} = 0.49, R_{PXP} = 1.0, P_{RX2} = 1.0)

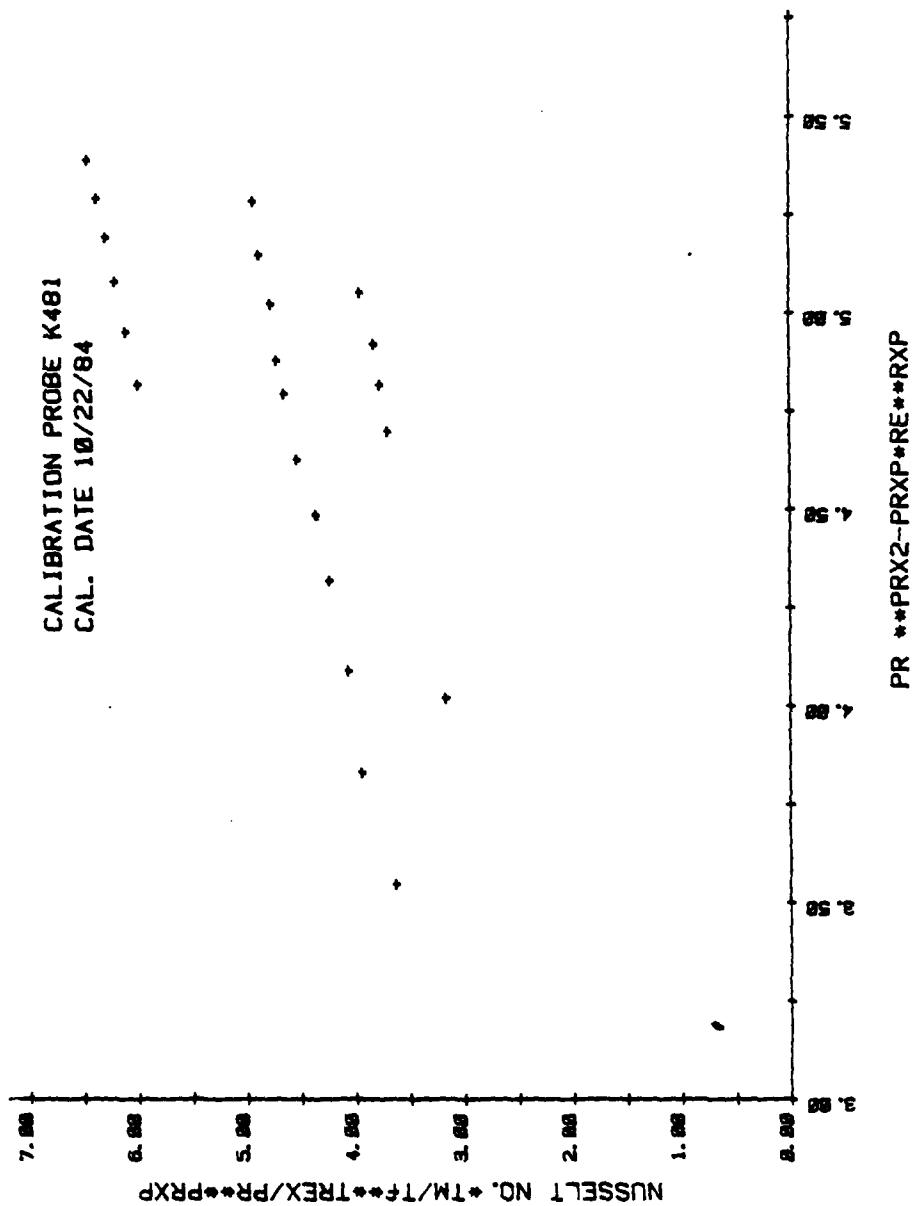


Fig 19. Hot-Wire Calibration Plot for Probe K481 Showing
74°F, 175°F, and 275°F Temperature Ranges.
(TREX = 1.0, RXP = 0.49, PRXP = 1.0, PRX2 = 1.0)

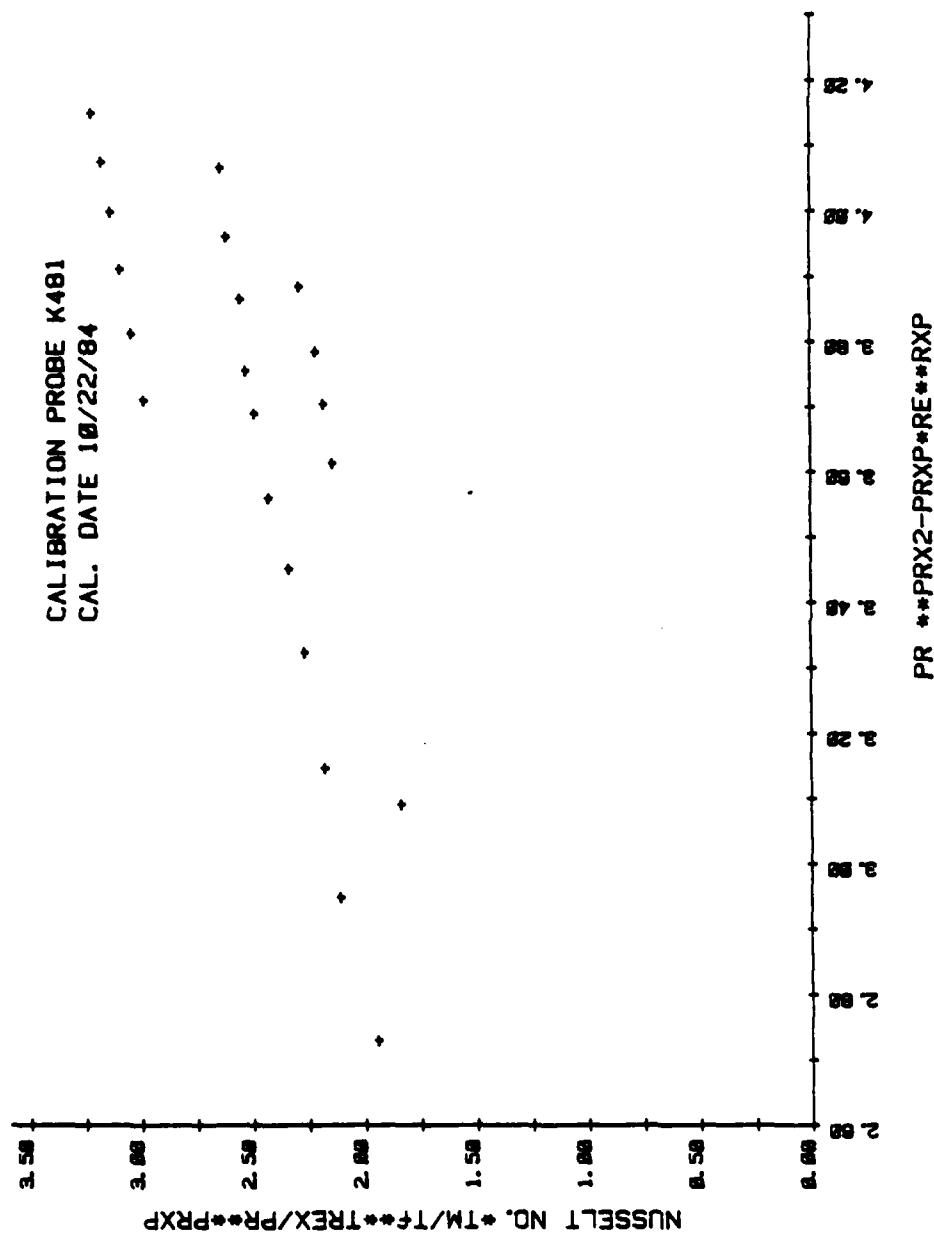


Fig 20. Hot-Wire Calibration Plot for Probe K481 Showing
74°F, 175°F, and 275°F Temperature Ranges.
(TREX = 0, RXP = 0.5, PRXP = 0.2, PRX2 = 0.9)

crossover point seems necessary to locate the most accurate configuration of exponents used to collapse the calibration data to a single, collapsed-linear curve as shown in figure 21. Probe K481 collapsed to a nominal 5% deviation from linear with maximum deviation of 11.03% when the temperature loading factor with $TREX = -2.03$ was applied. This spans 74-275°F from 389 to 896 ft/s. If we restrict the "usable" calibration only to the practical range used in the shock tube, that is discounting the 74°F data, the maximum error falls to 7.9%. The success of reducing all calibration data seemed most dependent on the correlation of slopes between individual temperature calibration curves. The slopes were 0.229 (74°F), 0.271 (175°F), and 0.341 (275°F) for probe K481. The error is primarily attributable to the differences in slopes between each calibrated temperature curve. Error within individual temperature calibrations, as determined from deviation from the ideal linear temperature versus resistance relationship from equation (1), was another major source of accuracy loss when the final collapsed-linear curve was reduced. Results of the K481 collapsed-linear calibration are presented in figure 21 while individual calibrations for each temperature range are presented in figures 22, 23, and 24. It can be seen from figure 22 that good linearity was achieved for the 74°F calibration. Deviation from linear was less than

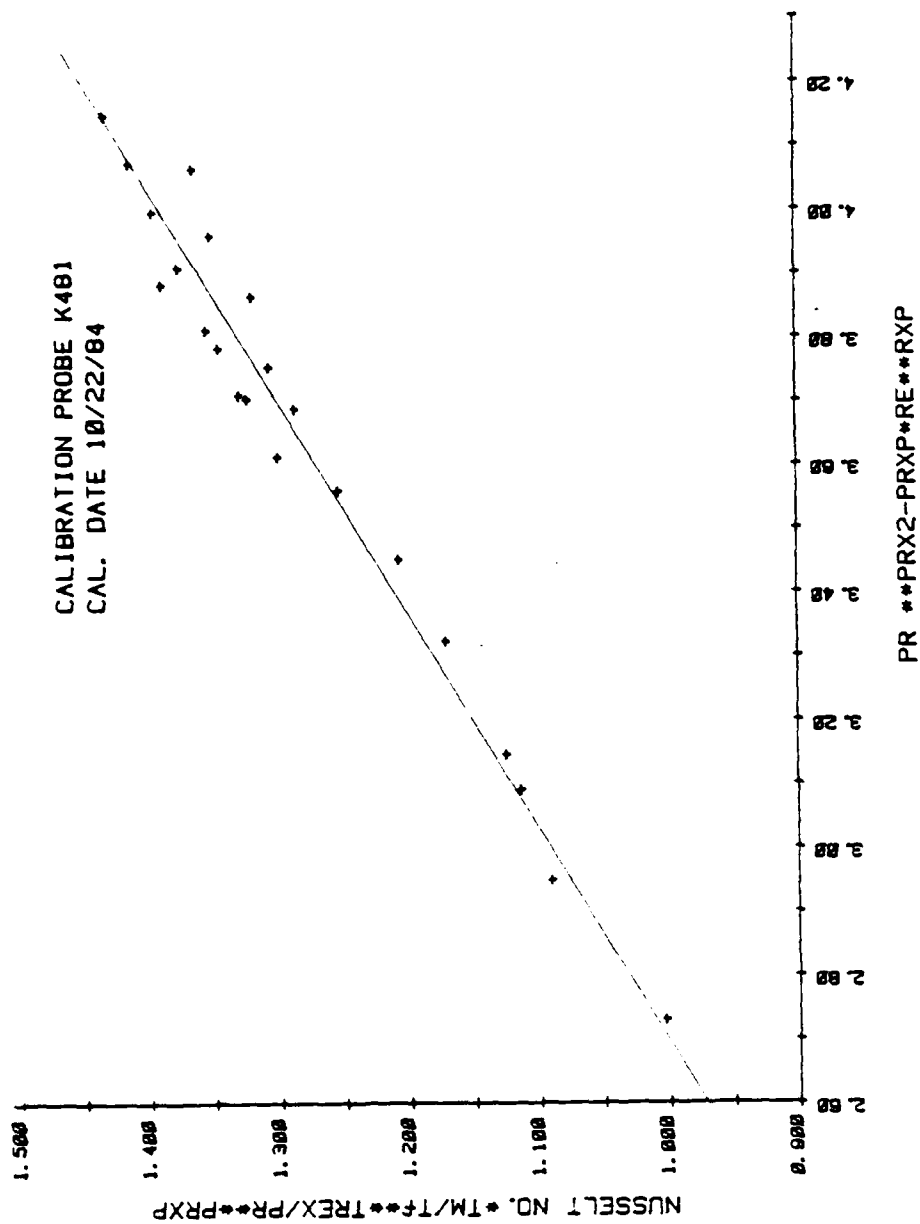


Fig 21. Hot-Wire Calibration Plot for Probe K481 Showing
74°F, 175°F, and 275°F Temperature Ranges in "Collapsed-Linear"
Form. (TREX = -2.03, RXP = 0.49, PRXP = 0.2, PRX2 = 0.9)

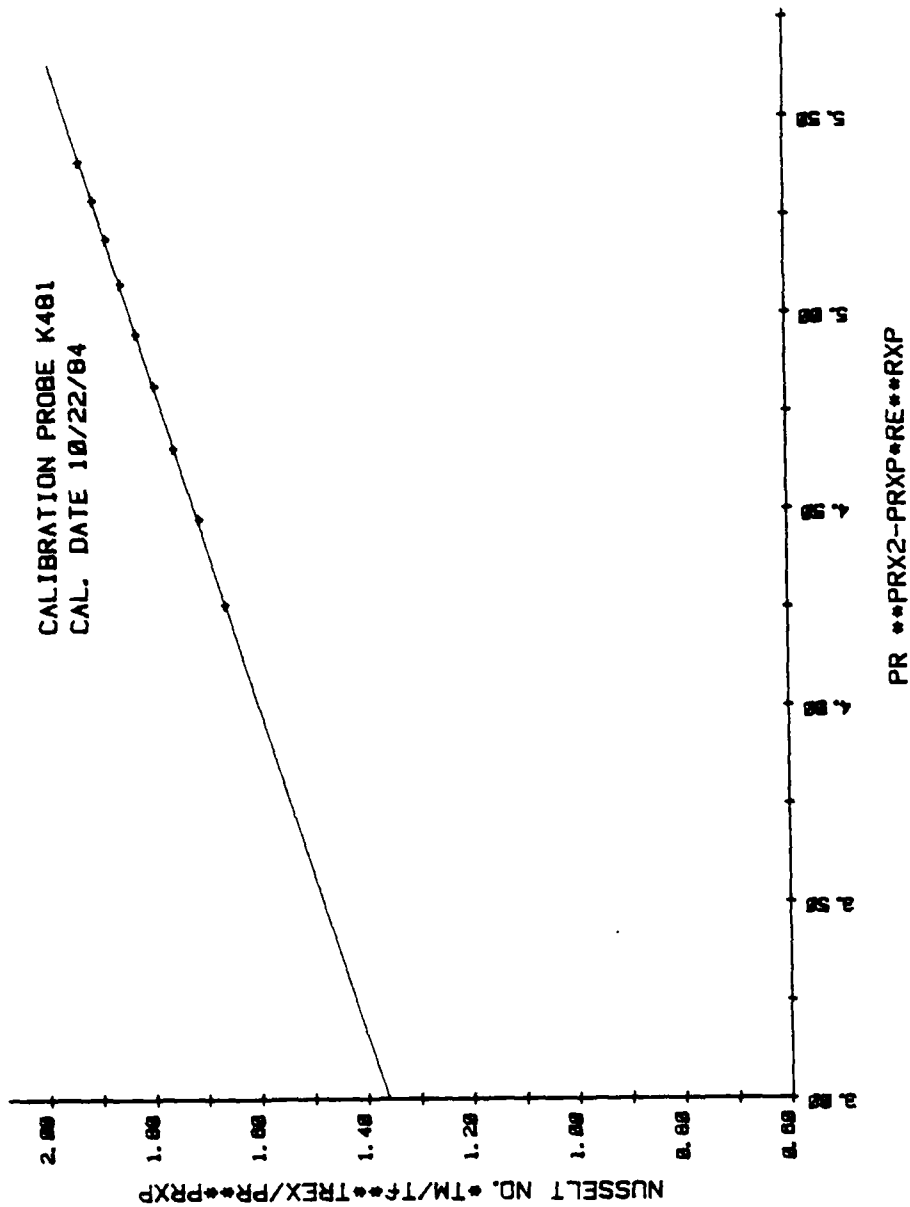


Fig 22. Hot-Wire Calibration Plot for Probe K481 Showing
74° F Temperature Range.
(TRES = -2.03, RXP = 0.49, PRXP = 1.0, PRX2 = 1.0)

HOT-WIRE ACCURACY

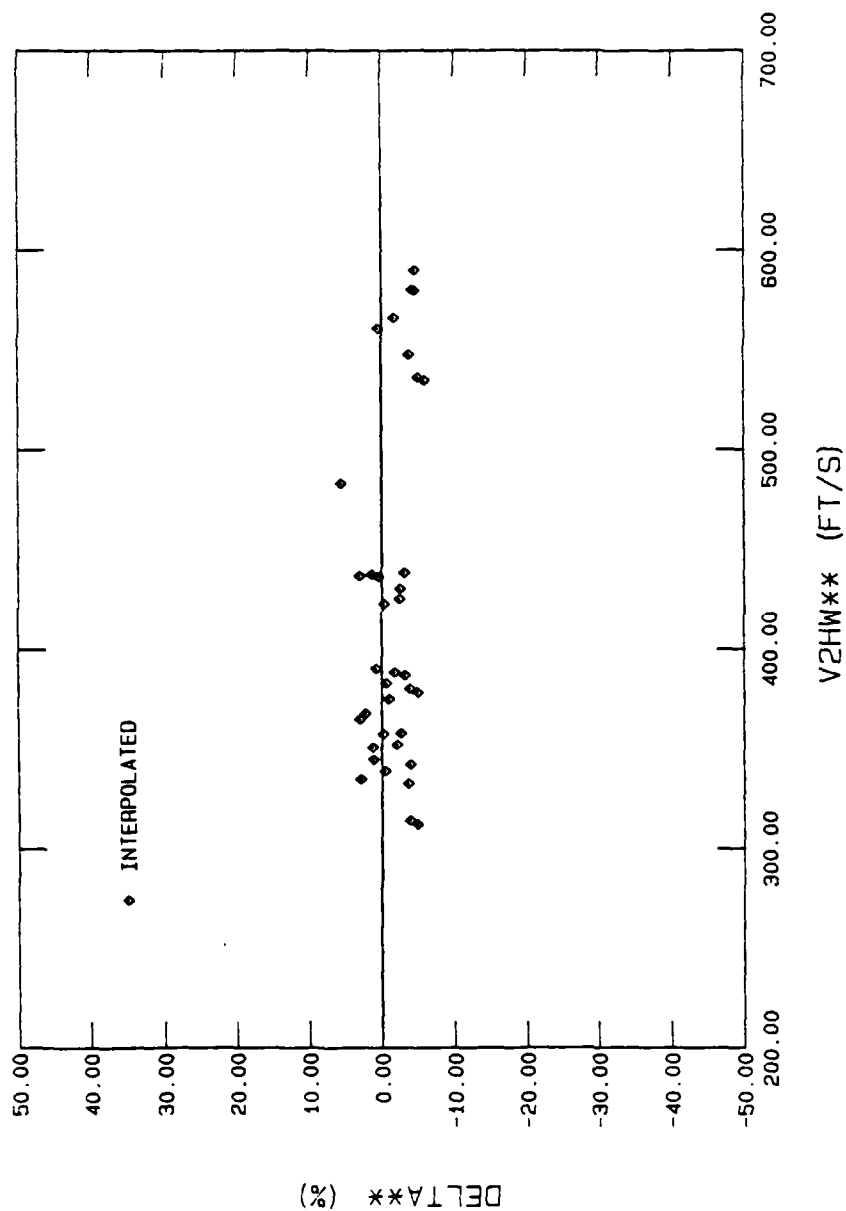


Fig 35. Accuracy of Hot-Wire Measured Velocity (Interpolated Calibration) vs. Actual Velocity Behind the Incident Shock Wave.

HOT-WIRE ACCURACY

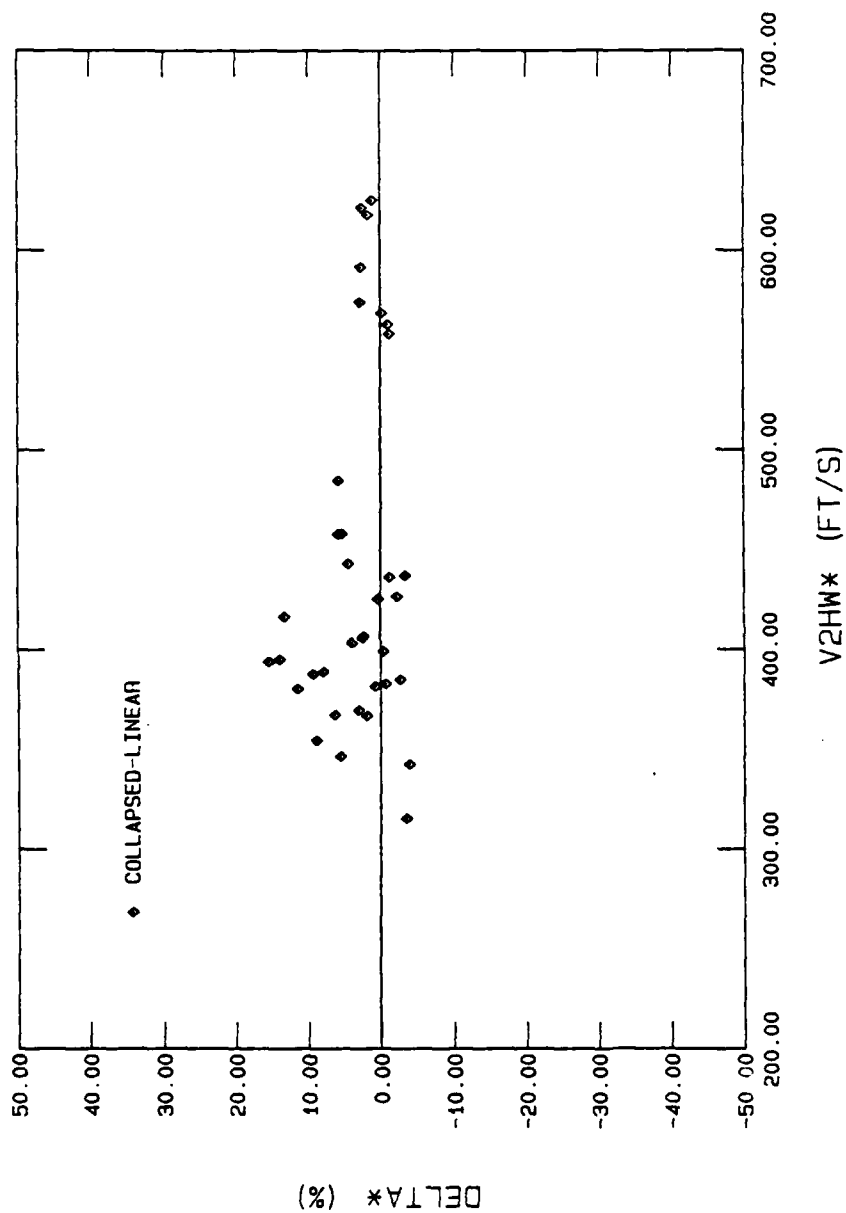


Fig 34. Accuracy of Hot-Wire Measured Velocity (Collapsed-Linear Calibration) vs. Actual Velocity Behind the Incident Shock Wave.

AIR VELOCITY BEHIND SHOCK

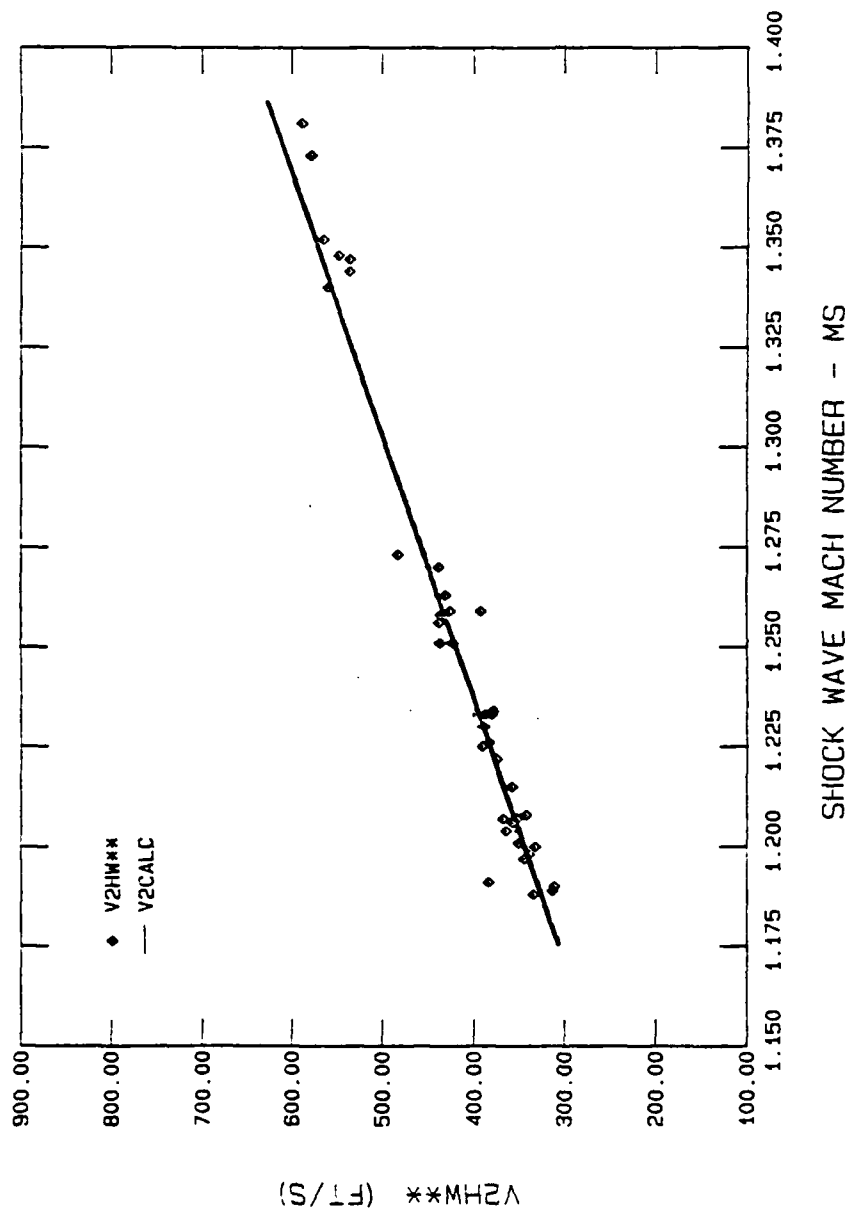


Fig 33. Velocity of Air Behind Incident Shock Wave Measured by Hot-Wire (Interpolated Calibration) Compared to Actual Velocity.

AIR VELOCITY BEHIND SHOCK

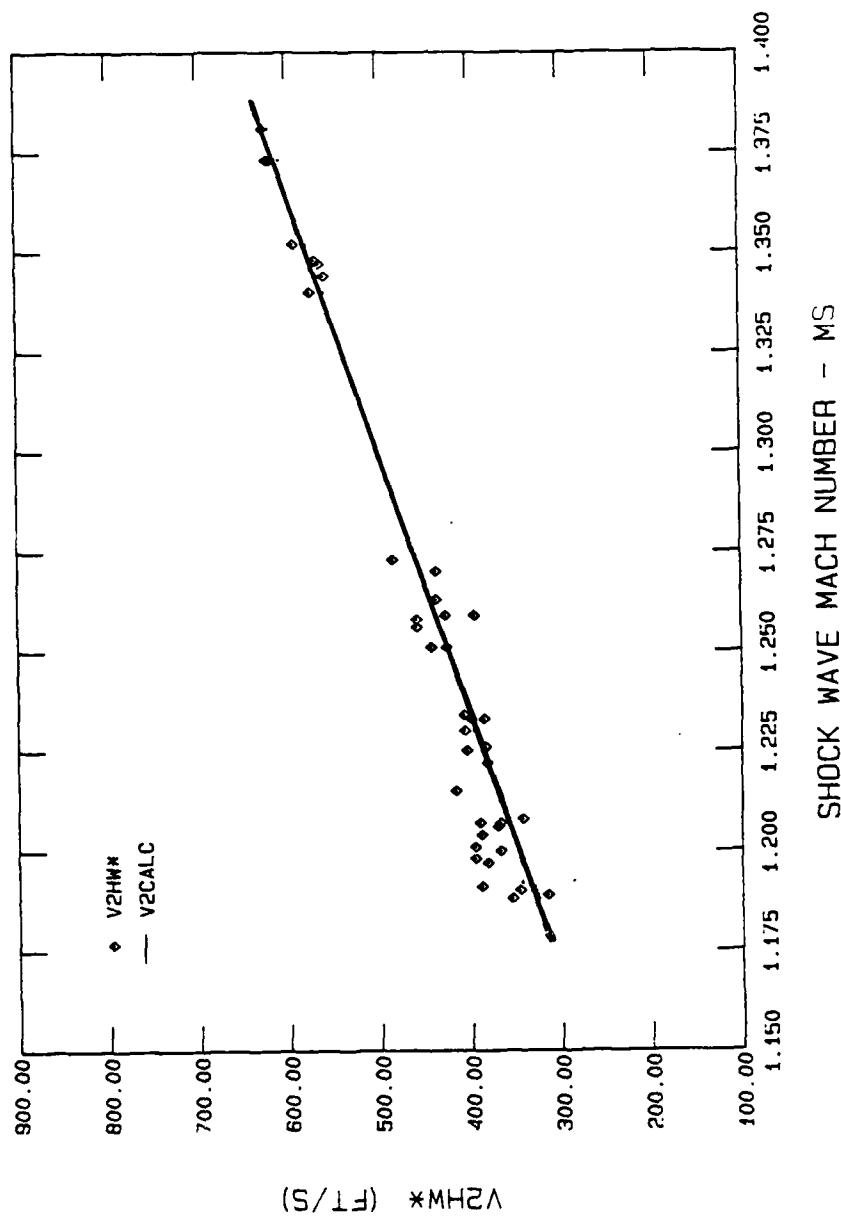


Fig 32. Velocity of Air Behind Incident Shock Wave Measured by Hot-Wire (Collapsed-Linear Calibration) Compared to Actual Velocity.

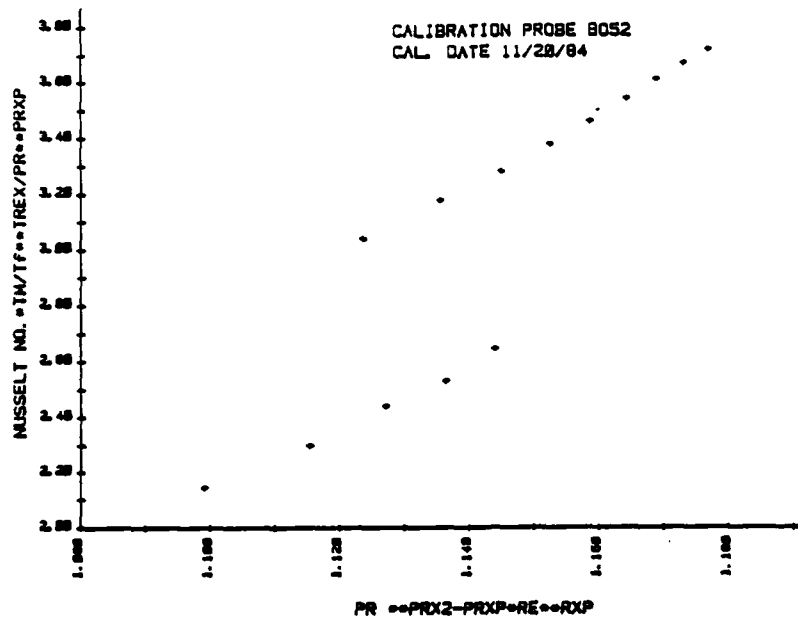


Fig 30. Hot-Wire Calibration Plot Showing 61°F and 175°F Temperature Range. (TREX = 0, RXP = 0.46, PRXP = 0.5, PRX2 = 0.8)

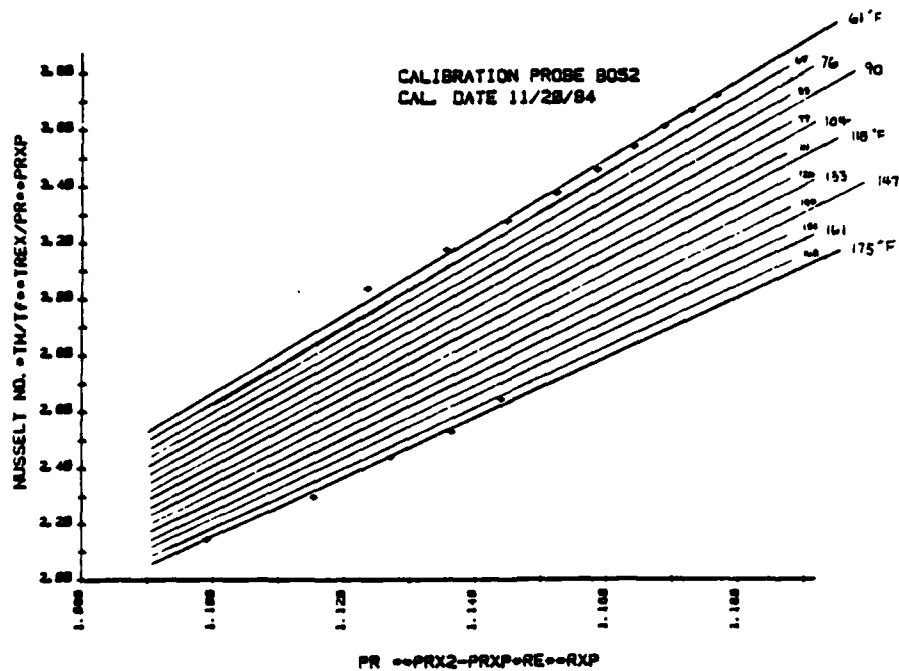


Fig 31. Hot-Wire Calibration Plot for Probe B052 Showing 61-175°F Temperature Range Ready for Interpolation. (TREX = 0, RXP = 0.46, PRXP = 0.5, PRX2 = 0.8)

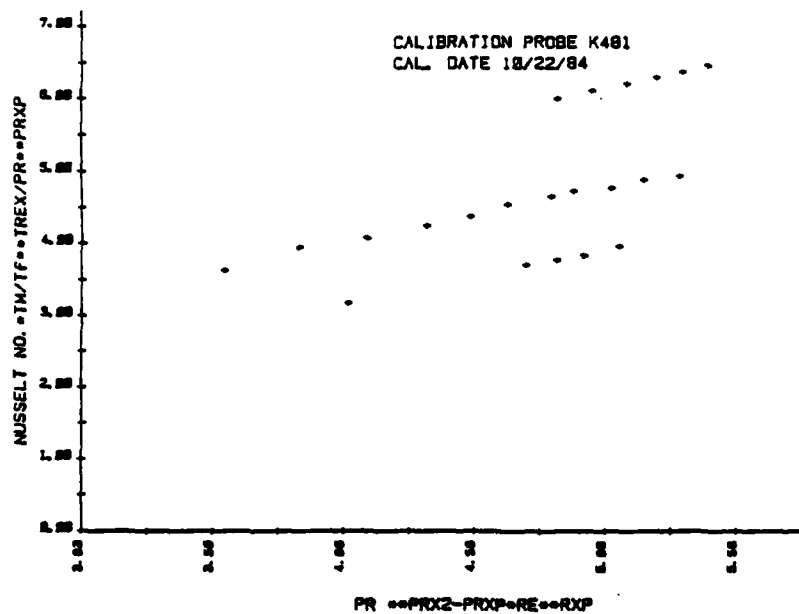


Fig 28. Hot-Wire Calibration Plot For Probe K481 Showing 74°F, 175°F, and 275°F Temperature Ranges. (TREX = 1.0, RXP = 0.49, PRXP = 1.0, PRX2 = 1.0)

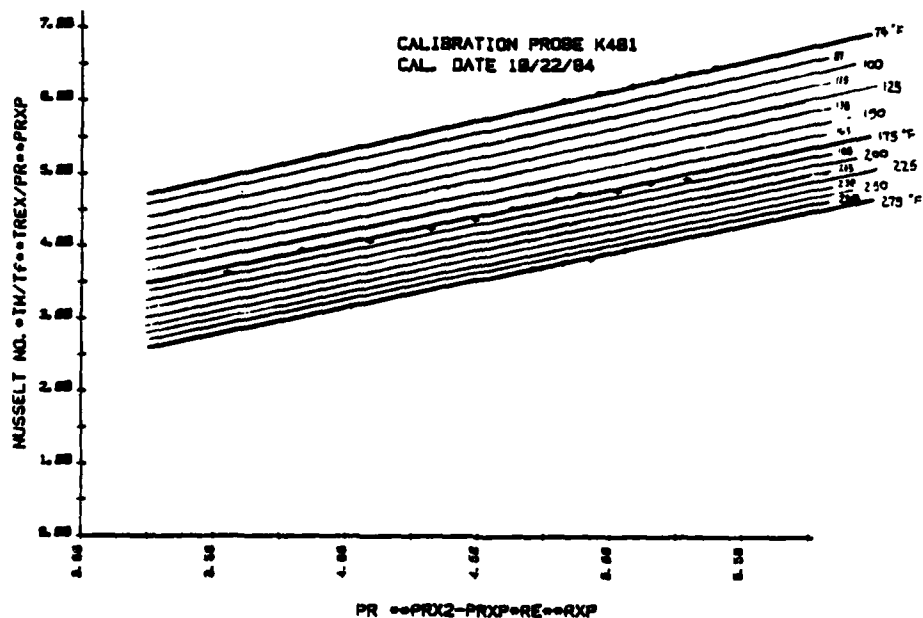


Fig 29. Hot-Wire Calibration Plot Showing 74-275°F Temperature Range Ready for Interpolation. (TREX = 1.0, RXP = 0.49, PRXP = 1.0, PRX2 = 1.0)

temperature curves and "filled in" intermediate temperature curves as shown in figures 28-31. Reynolds number and hence velocity were determined from the calibration plots by interpolating between temperature curves once the Nusselt number and fluid temperature were known. Actual velocities, determined from shock tube testing (V_{2calc}) ranged from 292 to 618 ft/s over temperatures from 129° to 201°F. This was demonstrated using probe K481 which was calibrated up to 896 ft/s and 275° F. Hot-wire measured velocities are potted versus shock wave Mach number (M_s) in figures 32 and 33. Shock wave Mach numbers at test conditions measured with the hot-wire are presented in Table IV. It can be seen from these figures that a reasonable degree of repeatability was achieved. The error, DELTA, measured as a percent based on velocity reading, ranged from negligible to +15.5% deviation from V_{2calc} when using the single collapsed-linear curve. This is shown in figure 34 where it can be seen that the data spread covered a DELTA* of approximately -3.5% to +15.5%. DELTA* refers to that data reduced by the collapsed-linear method. The error was significantly reduced to a nominal 4-5% with maximum error occurring at -5.97% when the same raw data (voltage, temperature, and pressure) were applied with the interpolation method. Delta** refers to that data reduced by the interpolation method and is plotted in figure 35. These data are presented in Appendix C, Table III. Figure

The general calibration equations for probes K481 and B052, respectively, are,

$$\text{Nu}(T_m/T_f)^{-2.03} = A \text{Pr}^{.2} + B \text{Pr}^{.9} \text{Re}^{.49} \quad (25)$$

and,

$$\text{Nu}(T_m/T_f)^{-2.70} = A \text{Pr}^{.5} + B \text{Pr}^{.8} \text{Re}^{.46} \quad (26)$$

Shock Tube Experiment

Velocity. Velocity of the air behind the incident shock wave was determined by measuring the shock wave speed (from time counters and the distance between pressure transducers used to trigger the counters) and the temperature in region 1 (test section), and applying a transformation from shock fixed coordinates to laboratory fixed coordinates. This air velocity, $V_{2\text{calc}}$, was used as the reference velocity against which the hot-wire measured velocity, $V_{2\text{HW}}$, was compared for accuracy. The maximum error in $V_{2\text{calc}}$ as determined by the possible error in the time measured by the counters, was on the order of 0.5% of $V_{2\text{calc}}$. Two methods were used to determine $V_{2\text{HW}}$. The first used the collapsed-linear calibration curve as in figures 21 and 25 where a single calibration curve was used to determine all velocities over the temperature spectrum, and the second assumed an even temperature distribution between calibrated

CALIBRATION PROBE B052
CAL. DATE 11/20/84

PR **PRX2-PRXP*RE**RXP

NUSSELT NO. *TM/TF**TREF/PR**PRXP

2.78 2.50 2.25 2.00 1.75 1.50 1.25 1.00

2.78 2.50 2.25 2.00 1.75 1.50 1.25 1.00

Fig 27. Hot-Wire Calibration Plot for Probe B052 Showing 175°F Temperature Range. (T_{REX} = -2.7, R_{XP} = 0.46, P_{RXP} = 0.5, P_{RX2} = 0.8)

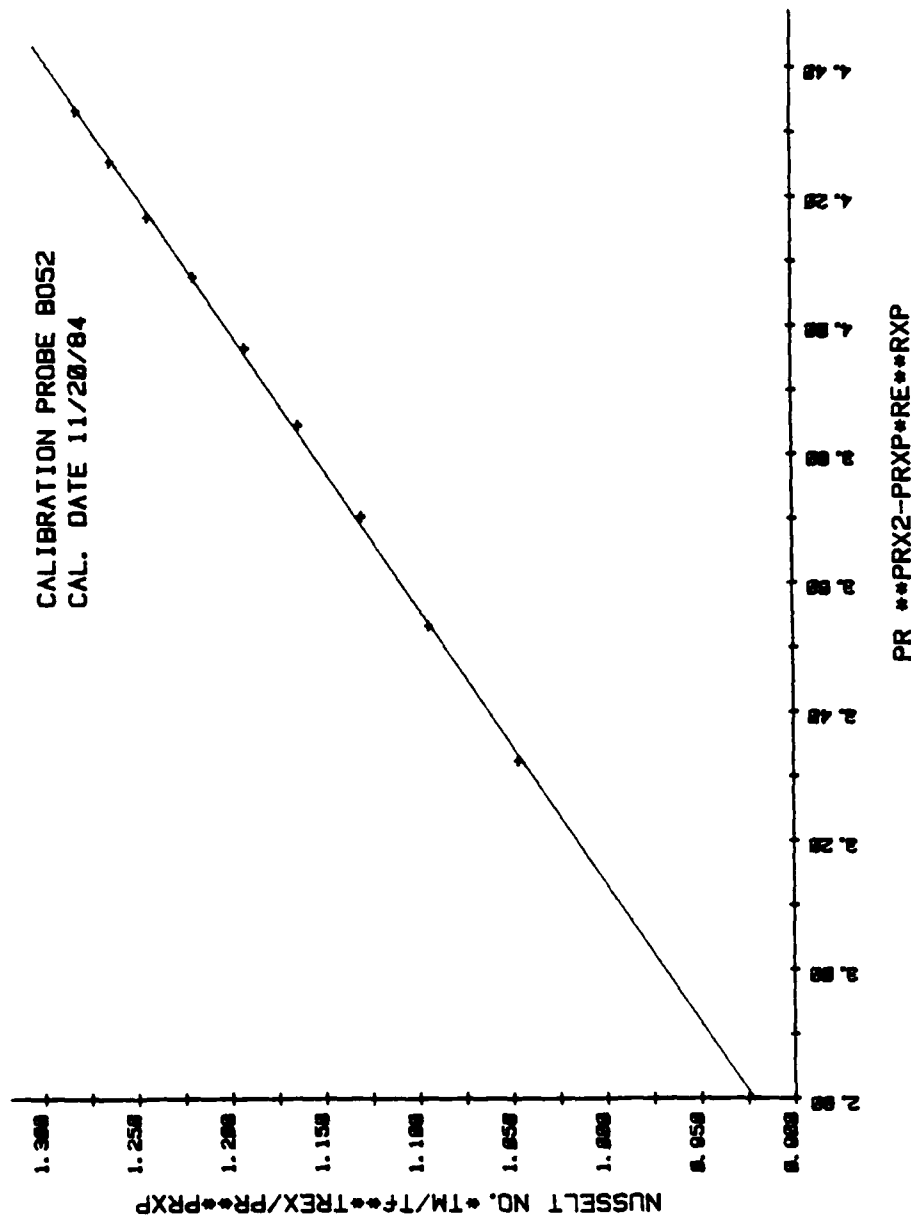


Fig 26. Hot-Wire Calibration Plot for Probe B052 Showing 61° F Temperature Range. (T_{REX} = -2.7, R_{XP} = 0.46, PR_{XP} = 0.5, PR_{X2} = 0.8)

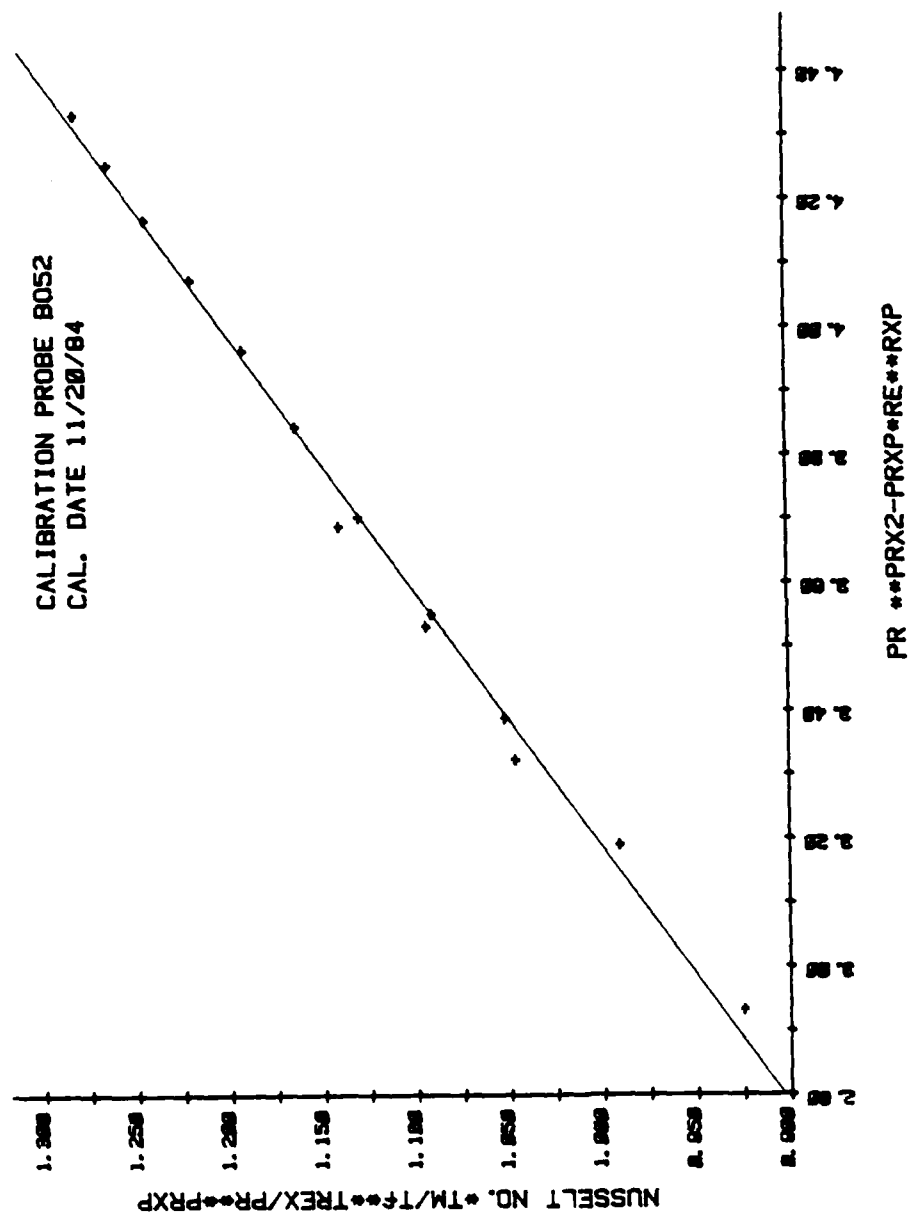


Fig 25. Hot-Wire Calibration Plot for Probe B052 Showing
61° F and 175° F Temperature Ranges in "Collapsed-Linear" Form.
(TREX = -2.7, RXP = 0.46, PRXP = 0.5, PRX2 = 0.8)

0.4%. The 175° F curve in figure 23 varied less than 2.7% from linear behavior nominally. The 275° F calibration curve varied less than 1%, and is shown in figure 24.

Probe B052 was calibrated at 61° F and 175° F from 382 to 736 ft/s. This probe was not calibrated higher than 175° F due to instability manifested in larger than normal voltage fluctuations during calibration which occurred at the higher fluid temperatures. Prandtl number exponents were determined to be 0.5 for PRXP and 0.8 for PRX2. The temperature loading factor exponent (TRES) found to give best results was -2.7. The "collapsed-linear" curve yielded average errors of less than 1% with a maximum error of 3.5% from linear. Slopes were on the same order as K481 with $B = 0.233$ (61° F) and 0.281 (175° F). Presumably, errors were less for B052 than for K481 because the temperature range over which the calibration took place was much reduced. The change in slope for the full range collapsing of temperature curves (61-175° F) was less than the full range change in slope for probe K481 (74-275° F). Slope change for probe B052 was 0.048 versus 0.112 for K481. Results of the B052 collapsed-linear calibration are presented in figure 25. Individual calibrations for the 61° F and 175° F temperature ranges are given in figures 26 and 27. It can be seen from figure 26 that good linearity was achieved at the 61° F calibration. Deviation from linear was nominally less than 0.5%. The 175° F curve resulted in less than 1% error.

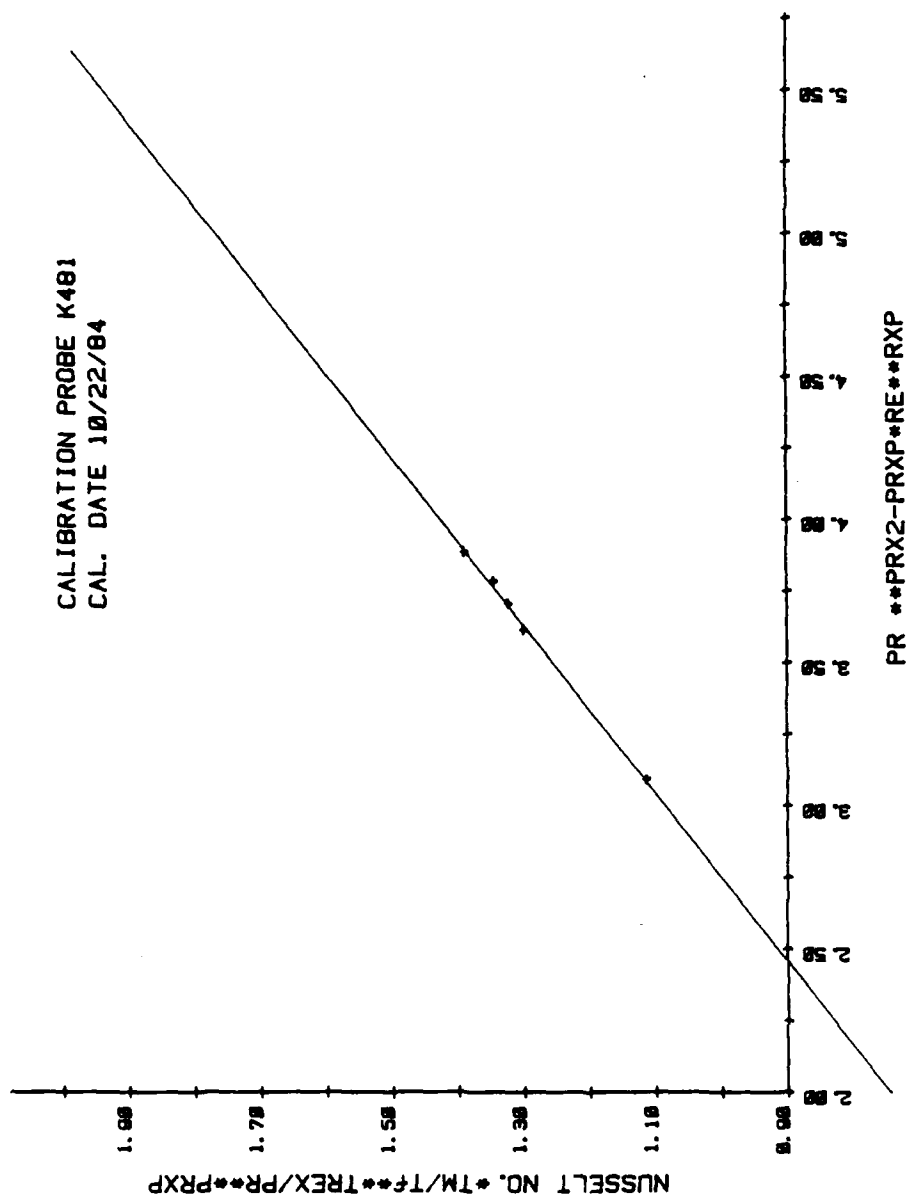


Fig 24. Hot-Wire Calibration Plot for Probe K481 Showing 275°F Temperature Range. (TREX = -2.03, RXP = 0.49, PRXP = 0.2, PRX2 = 0.9)

CALIBRATION PROBE K481
CAL. DATE 10/22/84

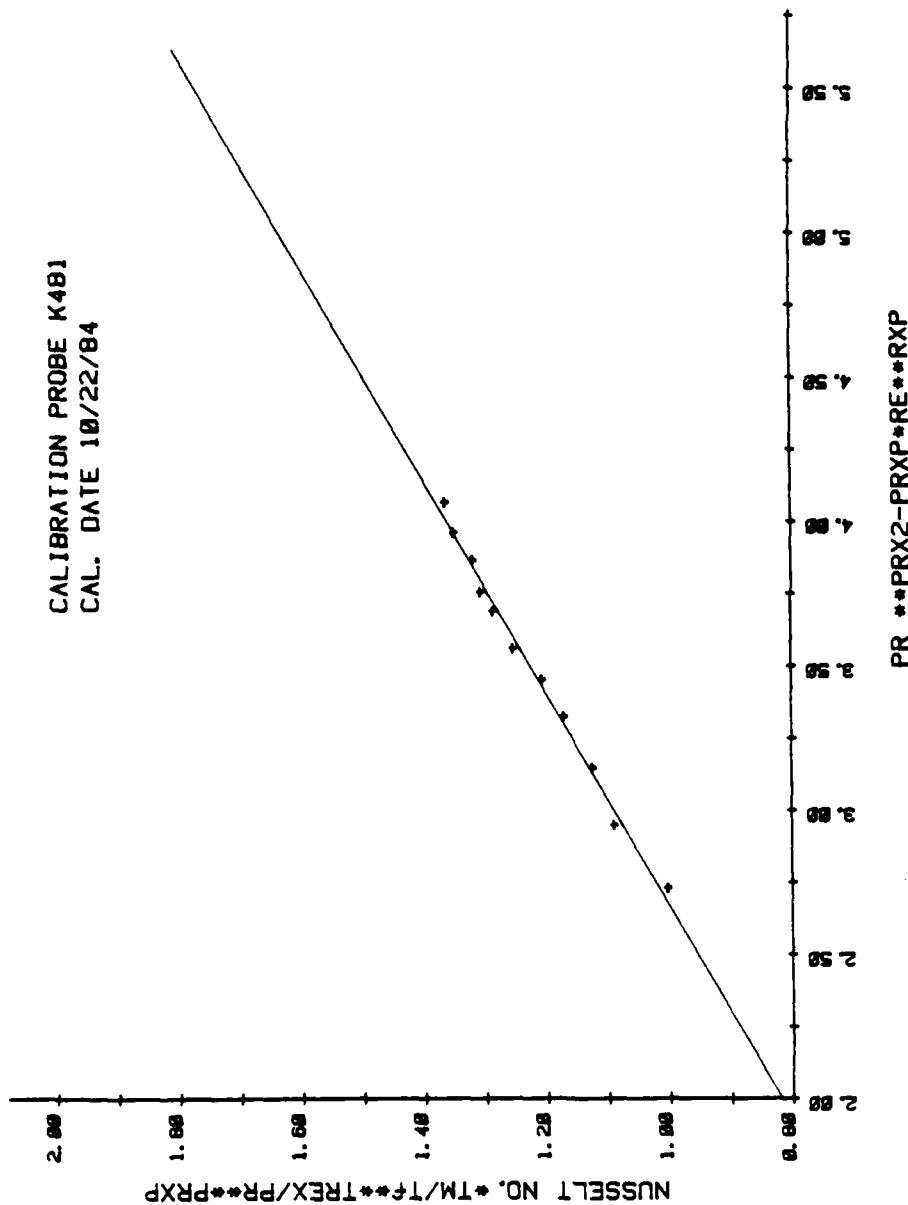


Fig 23. Hot-Wire Calibration Plot for Probe K481 Showing 175°F Temperature Range. (T_{REX} = -2.03, R_{XP} = 0.49, PR_{XP} = 0.2, PR_{X2} = 0.9)

HOT-WIRE ACCURACY

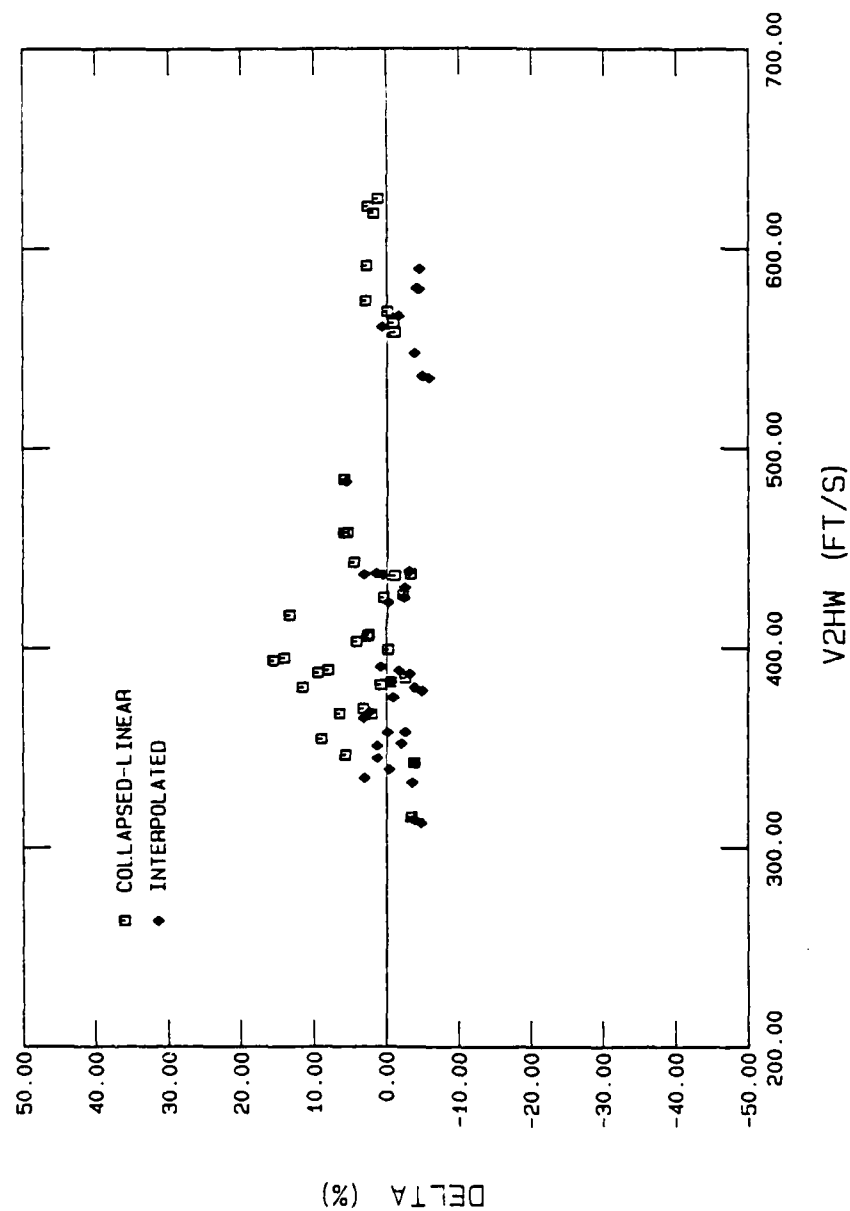


Fig 36. Accuracy of Hot-Wire Measured Velocity vs. Actual Velocity Behind the Incident Shock Wave.

36 compares velocity data for accuracy using collapsed-linear versus interpolated methods of hot-wire calibration. Note that some data presented are superscripted to indicate some test runs which experienced a diaphragm burst phenomenon (discussed later) and do not appear in figures 34 and 35.

Probe B052 achieved more promising results. It was calibrated over a lower temperature range (61° - 175° F) and yielded much better results with errors of 4% or better for both the collapsed-linear and interpolation methods. Velocities measured, ranged from 327 to 458 ft/s at corresponding temperatures from 134° to 162° F.

Kármán Vortex Streets. An objective of the research was to demonstrate the ability of the IFA-100 Intelligent Flow Analyzer to measure time variant velocities and their association with Kármán vortex Streets as they are produced from flow past a 3/16-inch circular cylinder. One might first question the existence of Kármán vortex streets in the region tested, 4 cylinder diameters downstream. Roshko (17) investigated wake development behind cylinders at Reynolds numbers from 40 to 10,000 in a low-speed wind tunnel. Many studies, including Roshko (17,18) and Morkovin (19) have shown that vortex street patterns are stable and well defined for long distances behind the cylinder when the range of cylinder based Reynolds numbers is from $40 < Re < 300$. It has also been demonstrated that periodic vortex shedding can occur past

$Re > 10^5$, but the free vortices are quickly dispersed by turbulent diffusion (Roshko) and a turbulent wake is established. Morkovin reports that from $300 < Re < 130,000$, a "laminar near-wake with single vortex street instability and secondary monocochlear vortices" is most likely to occur as shown in figure 37,

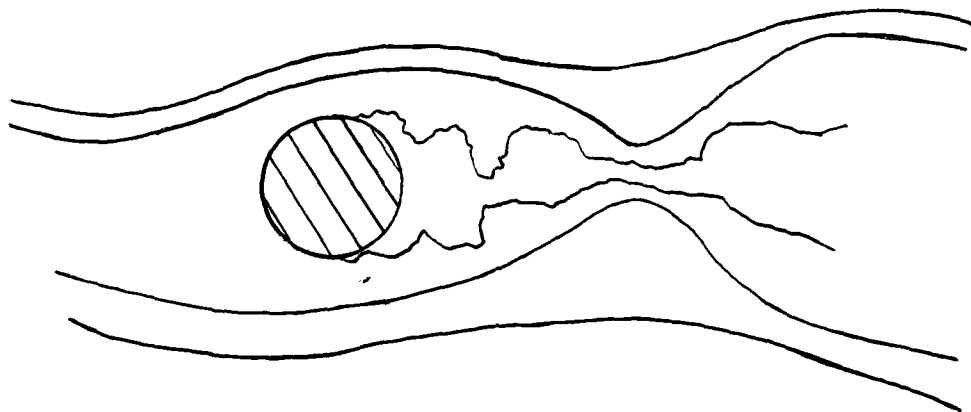


Fig 37. Laminar Near-Wake with Single Vortex Street Instability for $300 < Re < 130,000$.

One measure of Kármán vortex street formation is with the dimensionless Strouhal number,

$$S = fd/V \quad (27)$$

where

f = shedding frequency (from one side of the cylinder)

d = cylinder diameter

and,

V is the freestream velocity

A well defined relationship exists between the Strouhal number and Reynolds number. Figure 38 shows the relationship.

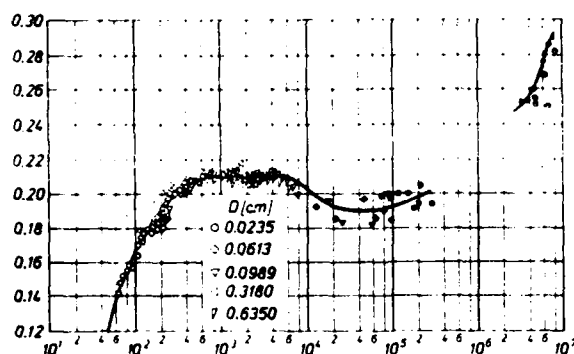


Fig 38. Strouhal Number as a Function of Reynolds Number.

Roshko found the region of "best fit" by plotting a dimensionless frequency, F , versus Re , where

$$F = fd^2/\nu = S Re \quad (28)$$

where

f = shedding frequency

d = cylinder diameter

and

ν = kinematic viscosity

The relationship was within 1 percent of linear for
 $300 < Re < 2000$ where,

$$F = 0.212 Re - 2.7 \quad (29)$$

shown in figure (39).

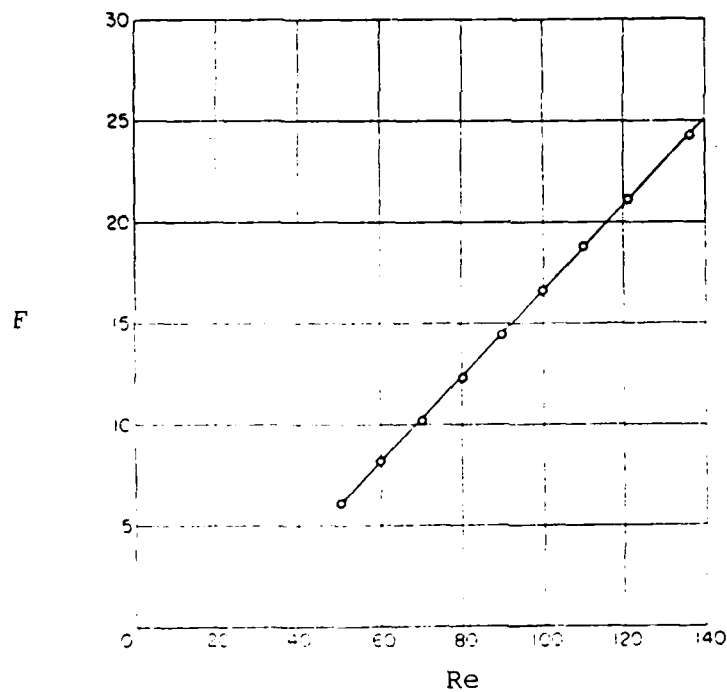


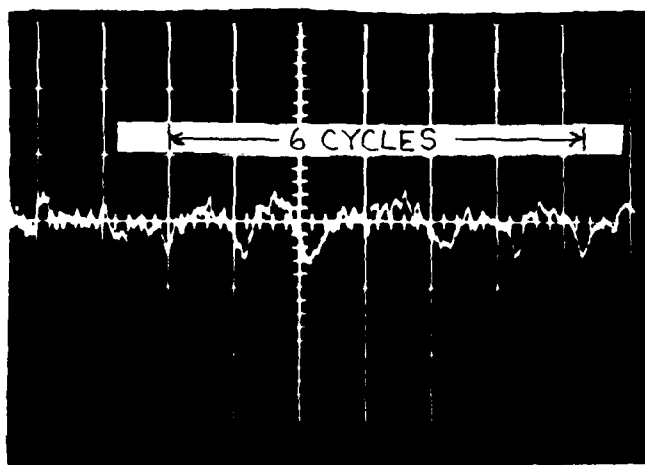
Fig 39. Nondimensional Frequency vs. Reynolds Number.

This corresponds to,

$$S = 0.212(1 - 12.7/Re) \quad (30)$$

Roshko also found that for Re up to 10,000, maximum error to the best fit line was 4 percent.

Reynolds numbers for data measured for fluctuating velocity in the shock tube ranged from 23,000-35,000. If one extends Roshko's linear relation between frequency and Reynolds number for $23K < Re < 35K$, error should be roughly on the order of 5 percent. This equates to an effective range of predicted Strouhal numbers based on equation (30) of $0.201 < S < 0.222$ for the measured shock tube data. This is the range of Strouhal numbers one would expect to find associated with irregular, unstable, Kármán vortex street formation for the shock tube experiment. Figure 40 which shows the conditions behind the shock tube cylinder, indicates some semblance of periodicity. An estimate of the number of "cycles", indicated between the arrows, was found to be nearly one cycle per division or approximately 5,000 Hz. This yields a Strouhal number of 0.207 which easily falls within the predicted range indicated above. It is surmised that the recorded signal does not indicate true, random turbulence, but rather an irregular, quasi-periodic vortex laden "street."



Run 028/1
 $f = 5,000 \text{ Hz}$
 $d = 3/16\text{-inch}$
 $V = 378 \text{ ft/s}$
 Sweep = $200 \mu\text{s/div}$
 rate

Fig 40. Photograph of an Oscilloscope Trace Showing Flow Conditions Behind the Cylinder in the Shock Tube.

Velocity fluctuations, as computed with the conventional form of turbulence intensity given in equation (5), ranged from 1.75 to 9.52 percent for the range of conditions measured in the shock tube. These fluctuations, plotted as turbulence intensity levels are shown in figure 41. Data is presented in Appendix C, Table V.

Pressure. Pressures measured with absolute pressure transducers ranged from 20.9 to 30.3 psia and are compared to the theoretical pressure determined from shock tube equations (2). Excellent correlation between measured and derived pressures was attained. Percent deviation between

the two was less than 2.7% for the worst case and less than 1% nominally. Experimental and theoretical pressure data (P_2/P_1) are compared at various Mach numbers in figure 42.

Mylar Burst Phenomenon. A problem was discovered during shock tube testing which biased the hot-wire anemometer signals in certain cases. The physical phenomenon, hereafter referred to as the Mylar burst phenomenon, was first noticed in the photographs taken which recorded voltages used in determining velocity behind the incident shock wave. As discussed in Section V, the method used to record voltages included setting the oscilloscope sweep to a reference grid line as shown in figure 9. As shown in figure 43, taken using a Transient Response Recorder, a signal perturbation occurred which biased the recorded signal in a positive voltage direction from the reference grid line. The magnitude of the voltage gave rise to significant errors in determining velocities when this condition occurred. This phenomenon was traced to a particular test condition where the double-diaphragm mode (Section II) was used at near the burst point for the particular thickness of Mylar used. It occurred each time the driver pressure was at or near 45 and 85 psia which corresponds to the driver pressure (P_4) that just breaks the .001 and .002-inch thick Mylar used during the testing. Figure 44a shows a small

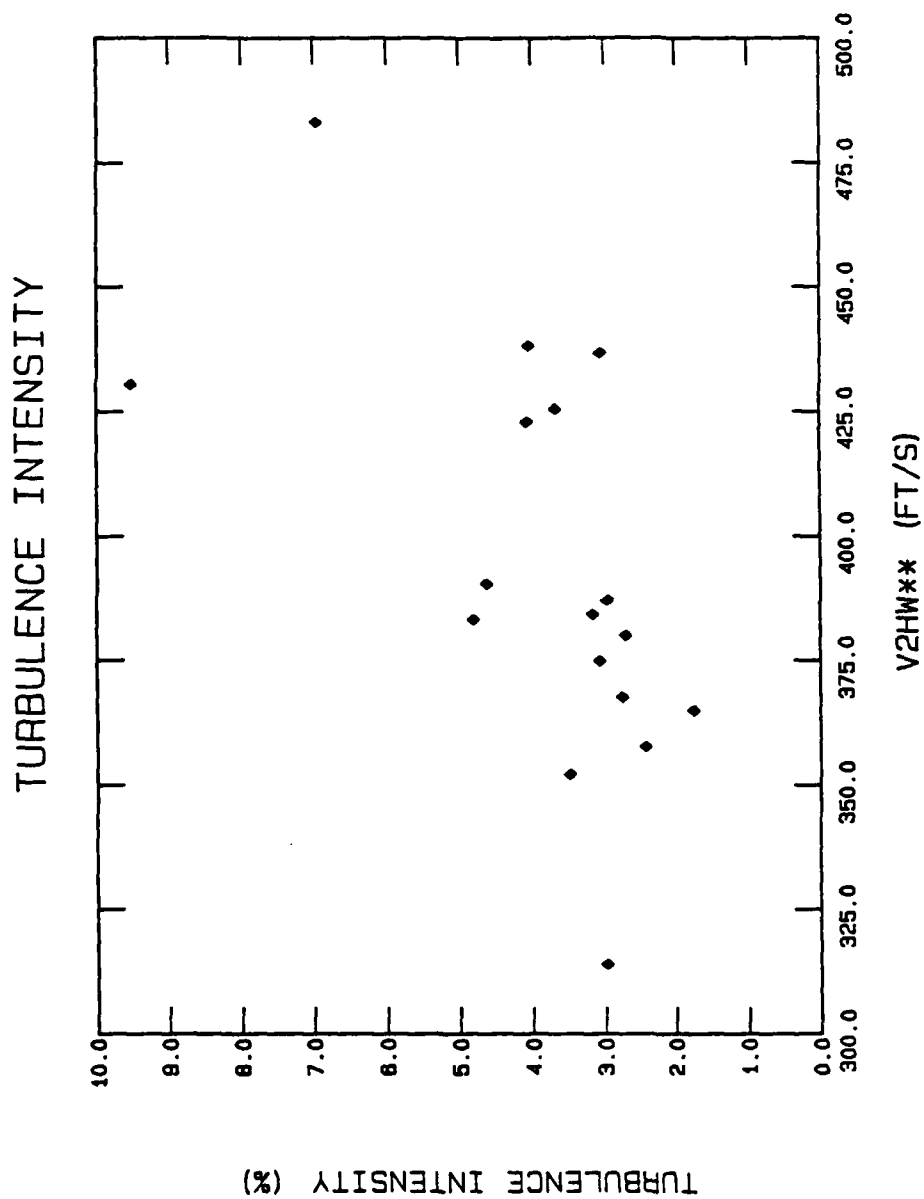


Fig 41. Turbulence Intensity as an Approximation to Velocity Fluctuations Behind the Cylinder in the Shock Tube.

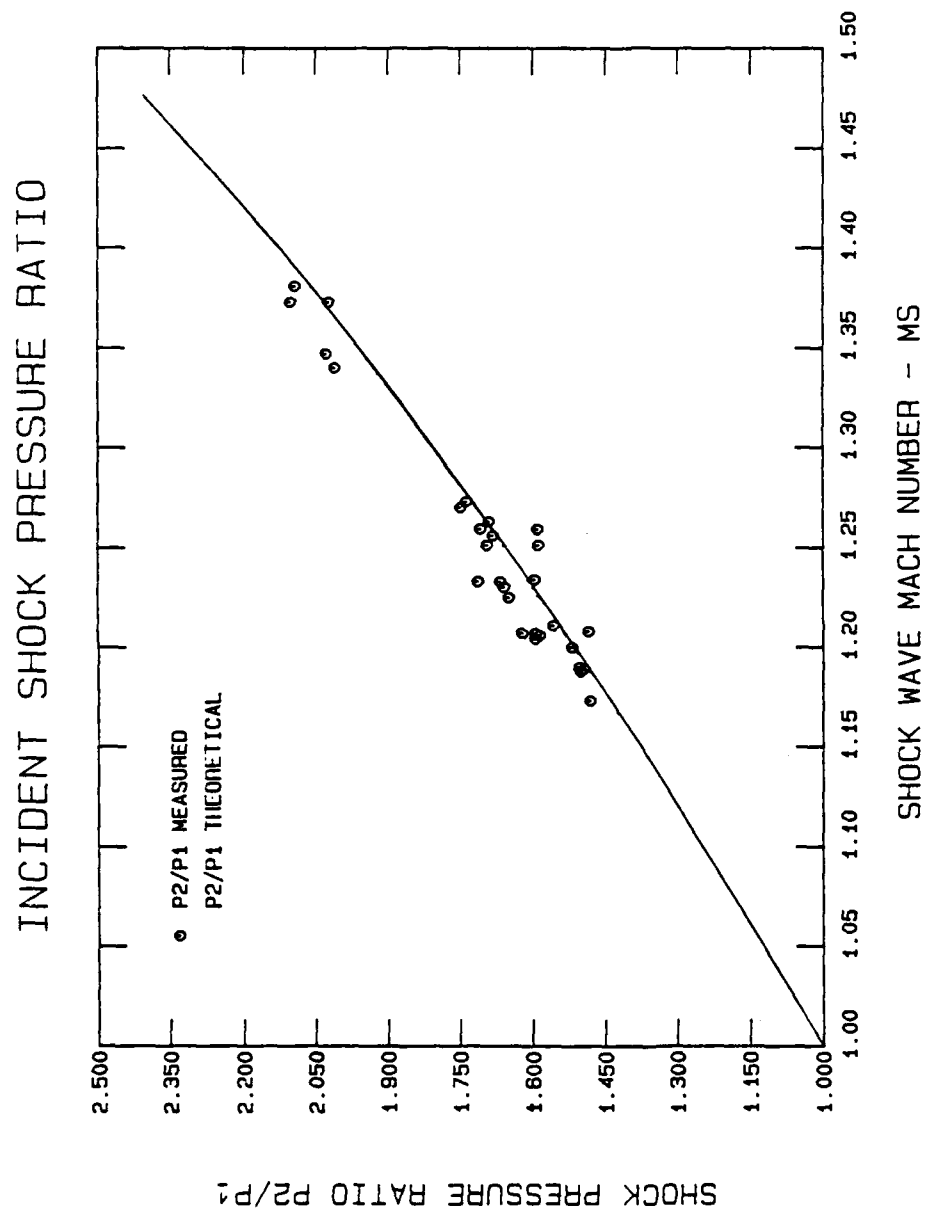
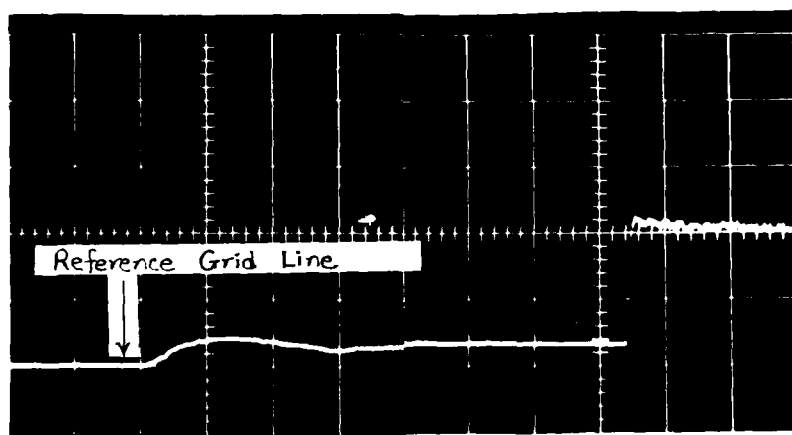


Fig 42. Incident Shock Experimental Pressure Data Compared to Theory (Ref. 2).

perturbation of the anemometer signal prior to shock passage while figure 44b shows a pronounced perturbation. The perturbation is probably the result of a pressure wave with a small pocket of air arriving at the hot-wire prior to incident shock arrival. The pressure wave could be formed during the shock firing sequence. After the downstream diaphragm (double-diaphragm mode) is stretched under initial pressurization to one-half operating pressure, the region between the diaphragms is isolated. The driver section is further pressurized to the desired operating pressure, and the center section is evacuated, causing the downstream diaphragm to relax. The upstream diaphragm then ruptures, and restretches the downstream diaphragm. However, there is a finite time for the downstream diaphragm to burst since the driver pressure corresponds to the minimum pressure required to rupture the Mylar. During this time, the downstream diaphragm has forced a pocket of air downstream past the hot-wire. The downstream diaphragm then bursts, with the resulting shock wave reaching the hot-wire after the pressure wave. As can be seen from figure 43, a rise of nearly 0.18 volts from the reference grid line occurs prior to shock passage. Voltages measured for the test runs experiencing this phenomenon are taken from the reference grid line and are presented in Tables II and III. These data are indicated by the superscript # and



V.T.S.=200 μ s/div

V.V.S.=0.5 V/div

Fig 43. Photograph of Oscilloscope Traces Showing the Mylar Burst Phenomenon.

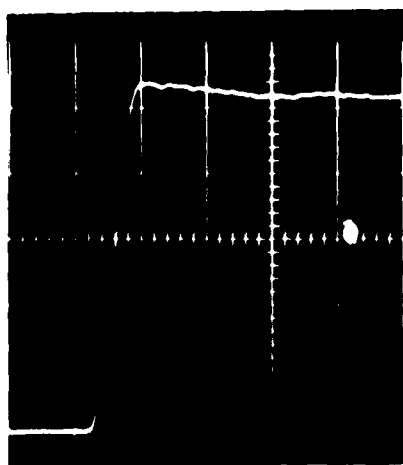


Fig 44a.

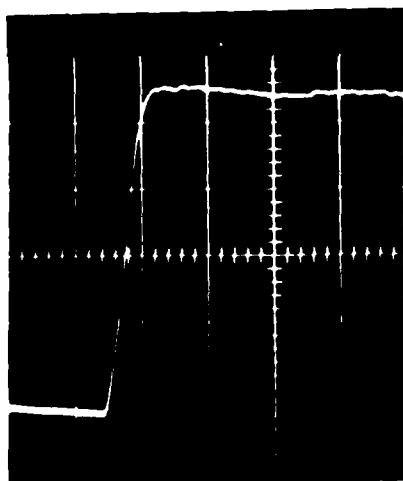


Fig 44b.

V.T.S.=20 μ s/div

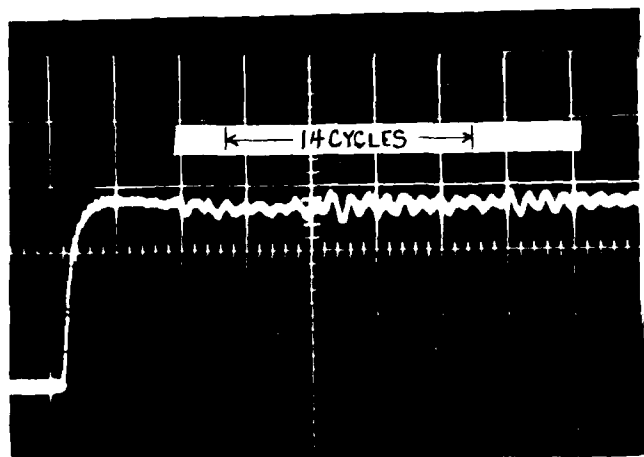
V.V.S.=0.2 V/div

Fig 44. Photographs of Oscilloscope Traces Showing (44a) Early Stage Perturbation Transition, and (44b) Pronounced Perturbation Due to the Mylar Burst Phenomenon.

are not included in figures 32 and 33 (velocity plots), due to the nature of the low hot-wire sensitivity (velocity/voltage) and the associated uncertainty in the actual reference of the voltage baseline.

Hot-Film Mechanical Resonance. A TSI 1214-10 hot-film sensor was initially used to demonstrate the ability of the IFA-100 Intelligent Flow Analyzer system to measure fluctuating velocity behind a cylinder in a shock tube. Structural vibration, not experienced with TSI 1210 and 1214-T1.5 hot-wires negated any possibility of this measurement with the TSI 1214-10 hot-film sensor. When the vibration occurred, the output signal recorded by the oscilloscope included harmonic perturbations which were of equal or greater magnitude than that of the turbulent velocity component in the direction of flow. Figure 45 presents a Transient Response Recorder conditioned anemometer signal showing the harmonic nature of the vibration.

The frequency of vibration is approximately 21,053 Hz as computed by the number of cycles (14) indicated by the arrows and sweep rate in figure 45. An analysis of mechanical vibration inducing resonant frequencies using a truncated cone (beam) gave a fundamental frequency of 22,134 Hz. The measured and analytical frequencies matched quite well indicating the presence of mechanical vibration. An analysis of mechanical vibration inducing resonant frequencies is given in Appendix B.



$$f = 21,053 \text{ Hz}$$

$$\text{V.T.S} = 175 \text{ } \mu\text{s/div}$$

Fig 45. Photograph of an Oscilloscope Trace Showing Mechanical Vibration Superimposed on a Hot-Film Signal.

AD-A154 694

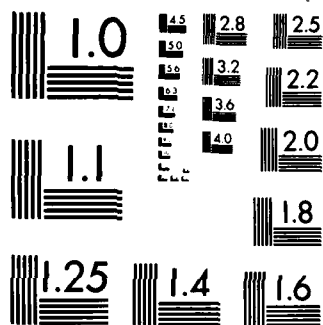
VELOCITY AND TRANSIENT MEASUREMENTS IN A SHOCK TUBE
USING A HOT-WIRE ANEMOMETER(U) AIR FORCE INST OF TECH
WRIGHT-PATTERSON AFB OH SCHOOL OF ENGI... S M MCQUEEN
DEC 84 AFIT/GAE/AA/84D-17 F/G 14/2

2/2

UNCLASSIFIED

NL





MICROCOPY RESOLUTION TEST CHART
NATIONAL BUREAU OF STANDARDS-1963-A

VII. Conclusions and Recommendations

A study was accomplished to demonstrate the ability of the IFA-100 Intelligent Flow Analyzer system to measure the average velocity and turbulence intensity behind the incident shock wave in a shock tube. In order to do this, a calibration technique was devised to encompass the broad spectrum of temperatures and velocities encountered in the shock tube environment. Two calibration methods, a collapsed-linear method, and an interpolated method, were employed in an attempt to optimize the procedure necessary to obtain the most accurate results.

Conclusions

1. In order for a hot-wire calibration to encompass the range of temperatures and velocities encountered in a shock tube, multiple calibrations at discrete temperatures which bound the testing range are required.

2. The most accurate method of calibration, designed to resolve velocity and turbulence intensity, involved interpolation between calibrated temperature curves.

3. The IFA-100 Intelligent Flow Analyzer is a suitable instrument for measuring velocity and turbulence intensity in the shock tube. Velocities measured ranged from 314 to 590 ft/s with 4 percent or better nominal accuracy using an interpolated calibration method.

Turbulence intensity measured 4 diameters downstream of a 3/16-inch diameter rod ranged from 1.75 to 9.52 percent.

4. Standard tungsten hot-wires, such as the TSI 1214-T1.5 and TSI 1210-T1.5 sensors used during testing, are not satisfactory for shock tube use. Calibration of the tungsten wires was limited to operating temperatures near 300° C which severely limited the voltage/velocity sensitivity required at the test conditions in the shock tube.

5. Hot-film sensors, such as the TSI 1214-10 probes used during testing, are unsuitable for measuring turbulence intensity in a shock tube. The impulsive forces generated from the shock wave induce a vibration in the probe supports which create voltage fluctuations in the anemometer output of the same order as the voltage changes induced by the turbulence being measured.

Recommendations

Based on the results of this study, the following recommendations are made:

1. High-temperature capable hot-wires, such as those constructed of platinum, should be used in shock tube applications. This is required in order to attain suitable voltage/velocity sensitivity for the higher temperatures and velocities encountered in the shock tube.

2. Calibration of hot-wires should cover only the specific range of testing to be accomplished. Increasing

the calibration range to include temperatures outside the specified testing range only serves to introduce error in data reduction.

3. To eliminate error introduced when data is measured directly from oscilloscope photographs, digitized data should be output directly from such support equipment as a Transient Response Recorder or digital oscilloscope via an RS-232 port. This will significantly reduce errors due to "man-in-the-loop."

Appendix A

Instrumentation

Table I gives a listing of pertinent test instrumentation and support equipment.

Figure 46 shows a schematic of the instrumentation and support equipment layout. Note that the item numbers in Table I correspond to the numbers shown in figure 46.

TABLE I
TEST INSTRUMENTATION

ITEM	DESCRIPTION	MODEL#	S/N	USE
1.	Tektronix oscilloscope	535A	029274	Display HW signal
2.	Tektronix oscilloscope	535A	022799	Display pressure P2
3.	Tektronix dual trace amplifier	1A1	023883	w/ item 1 above
4.	Tektronix dual trace amplifier	1A1	-----	w/ item 2 above
5.	TSI IFA-100 Flow analyzer	150	134D	Measure velocities and turbulence
6.	Shock tube control board	---	----	Control shock tube operation
7.	Ballantine oscilloscope	10668	0137	Match frequency response of calibration to test condition
8.	Marsh Bourdon tube pressure gauge (100 psig)	101	200	Set intermediate diaphragm burst pressure
9.	Ashcroft Bourdon tube pressure gauge (200 psig)	---	1377	Set driver pressure
10.	Marshall Bourdon tube pressure gauge (30"Hg vac.)	---	----	Set driven section pressure <Pambient
11.	U.S. Gauge Bourdon tube pressure gauge	---	1377	Set driven section pressure >Pambient
12.	Sorenson power supply	DCR/ 40-13B	1416	Power to shock tube control board
13.	HP Universal counter	5325B	1216	Shock wave timer
14.	CMC universal counter	726C	120363	Shock wave timer
15.	Polaroid camera	---	----	Photograph oscilloscope trace
16.	Polaroid camera	---	----	Photograph oscilloscope trace
17.	GHI Transient Response Recorder	VK220E	904498	Capture and store anemometer signal
18.	Omega Digicator Fe-C thermocouple	400B	5006952	Measure ambient temperature
19.	Endevco power supply	4225	AC13	Provide power to all pressure transducers
20.	Endevco signal conditioner	4423	AE77	Amplify pressure transducer signal
21.	Endevco signal conditioner	4423	AF01	Amplify pressure transducer signal

TABLE I (continued)

ITEM	DESCRIPTION	MODEL#	S/N	USE
22.	Endevco signal conditioner	4423	AE80	Amplify pressure transducer signal
23.	Endevco pressure transducer	8530A-100	TN07	Trigger oscilloscope sweep
24.	Endevco pressure transducer	8530A-100	TN05	Trigger counters on
25.	Endevco pressure transducer	8530A-100	TN08	Trigger counters off measure P2
26.	TSI hot-wire probe	1214-T1.5	K481	Sense velocity change

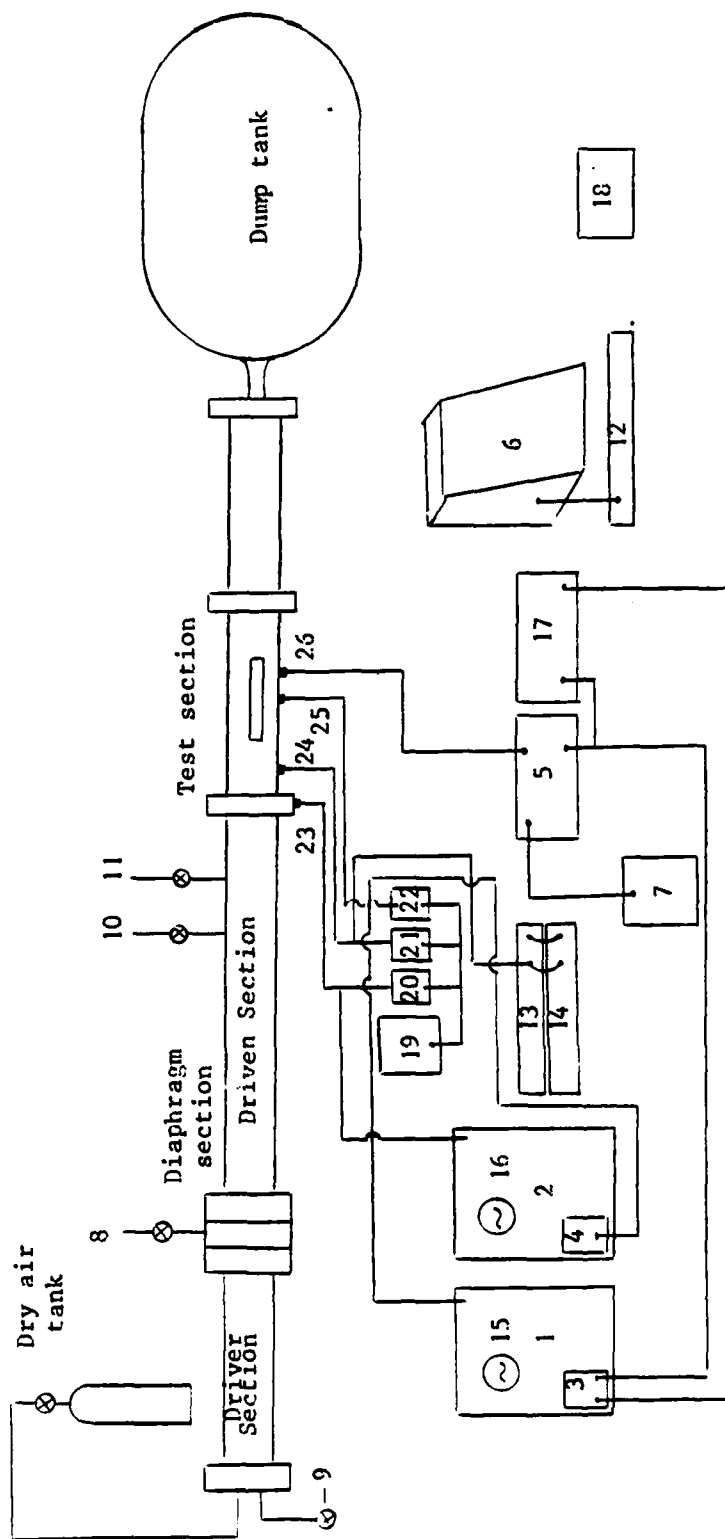


Fig 46. Schematic of Instrumentation and Support Equipment.

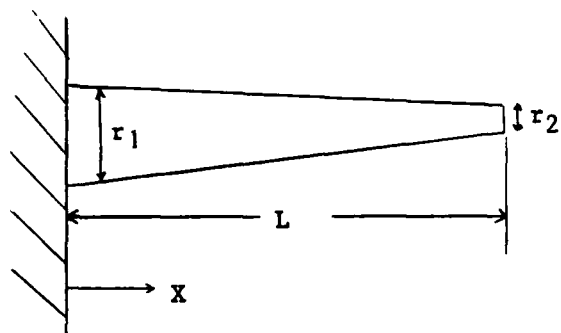
Appendix B

Hot-Film Mechanical Resonance

Natural frequencies of a freely vibrating elastic system can be modeled by equating the systems maximum potential energy to its maximum kinetic energy at an extreme configuration of the system. Rayleigh's principle (21,22) states that the estimated frequency of vibration of a conservative system, oscillating about the equilibrium position, has a stationary value in the neighborhood of a natural mode. The Rayleigh Energy Method given by equation (31), gives the fundamental frequency as,

$$\omega^2 = g \frac{\int_0^L EI(x) (d^2y/dx^2)^2 dx}{\int_0^L wy^2 dx} \quad (31)$$

This method was used to determine the resonant frequency of a hot-film probe when impulsively excited by a shock wave. The model used was a tapered beam (long, thin cone) as shown in figure 47, of radius $r(x)$ fixed at one end with the other end free to move subject to the following boundary conditions,



$$@ X = 0, \quad Y = Y' = 0$$

$$@ X = L, \quad Y'' = Y''' = 0$$

Fig 47. Truncated Cone Used to Model Hot-Film Mechanical Vibration.

$$r(x) = r_1 - (r_1 - r_2)X/L \quad (32)$$

A fourth-order polynomial, equation (33) was used to describe the expression for the dynamic elastic line, $Y(x)$ to solve for the fundamental mode.

$$C_4X^4 + C_3X^3 + C_2X^2 + C_1X + C_0 = Y(x) \quad (33)$$

The moment of inertia for a circular cylinder is,

$$I(x) = 1/4 r(x)^4 \quad (34)$$

The natural frequency of the hot-wire probe is determined by taking the appropriate derivatives (with respect to x),

applying the boundary conditions, and integrating using equation (31). Measured and derived properties of the "beam", modeled after a TSI 1214-10 hot-film probe are,

L - length, 0.255 in

r1 - base radius, 0.013 in

r2 - tip radius, 0.0025 in

E - modulus of elasticity, 28×10^6 KSI for stainless steel

W_{sp} - specific weight, 0.28 lbm/cu in

Using these properties, the fundamental frequency for this model was 22134 Hz. This agrees quite well with the frequency of vibration determined from the oscilloscope trace shown in figure 45, which was found to be 21,053 Hertz. The difference is probably due to the slight change in vibration characteristics of the tapered rod caused by the hot-wire attached to its tip. Additional differences are also attributable to measurement error and error due to approximation of mode shape, material properties, etc.

Appendix C

Test Data

Table II shows data used to determine actual versus measured air velocity behind the incident shock wave. The table includes data on (a) run identification, (b) voltage (E_s) recorded by the IFA-100 hot-wire anemometer system, (c) temperature behind the shock wave (T_2) taken from reference (2) as the computed temperature in region 2, (d) pressure behind the shock wave in region 2 (P_2) computed from theory in reference (2), and (e) the output device (oscilloscope = Osc, Transient Response Recorder = TRR) which recorded the voltages used to determine air velocities.

Table III shows data calculated from experimental and derived test data given in Table II (above). The table includes data on (a) run identification, (b) actual air velocity (V_{2calc}) computed from the measured shock wave speed (W_s) and ambient temperature in region 1, (c) air velocity as measured by the hot-wire using a collapsed-linear calibration curve (*), (d) air velocity as measured by the hot-wire using an interpolated set of calibration curves (**), and (e) respective errors measured in percent of deviation from V_{2calc} given from the following equation,

$$\text{DELTA}(\%) = \frac{(V_{2\text{HW}} - V_{2\text{calc}}) \times 100}{V_{2\text{calc}}} \quad (35)$$

These data are presented in figures 32-36.

Table IV shows measured and derived data including (a) run identification, (b) shock wave Mach number, (c) Reynolds number based on hot-wire diameter, (d) Nusselt number, and (e) Prandtl number.

Table V shows data used to compute turbulence intensity, the model used to determine levels of velocity fluctuation for the air behind the incident shock wave as the flow passes a 3/16-inch circular cylinder. Data in the table includes (a) run identification, (b) the AC rms voltage (E_{ac}), (c) the total DC voltage (E_t), (d) turbulence intensity as a percent, and (e) the air velocity as measured by the hot-wire anemometer using the interpolated method of reduction.

TABLE II

Measured and derived voltage, temperature, and pressure data used to determine velocity of air behind incident shock wave.

RUN	E _o (volts)	T2 (°F)	P2 (psia)	W _s (ft/s)	DEVICE	
					Osc	TRR
028/1	1.922	153.0	22.805	1377		x
028/2	1.941	152.1	22.695	1374		x
028/3#	1.941	153.3	22.842	1378		x
028/4	1.942	153.3	22.842	1378		x
028/5	1.919	153.3	22.842	1378		x
028/6	1.955	159.3	23.583	1398		x
028/7	1.957	161.1	23.807	1404		x
028/8	1.950	162.0	23.920	1407		x
N7/1	1.928	143.2	22.875	1372	x	
N7/2	1.908	138.8	22.324	1357	x	
N7/3	1.907	137.6	22.178	1353	x	
N7/4#	2.027	185.6	28.393	1514	x	
N7/5#	2.027	182.9	28.027	1505	x	
N7/6#	2.027	184.7	28.271	1511	x	
N8/1	2.088	197.9	29.886	1552	x	
N8/2	2.085	198.2	29.928	1553	x	
N8/3	2.087	200.9	30.304	1562	x	
N8/4	2.065	186.7	28.362	1515	x	
N8/5#	1.885	141.9	22.558	1365	x	
N8/6	2.074	190.9	28.934	1529	x	
N8/7	---	---	---	1413	x	
N8/8	1.989	158.9	24.692	1422	x	
N8/9	1.989	158.3	24.616	1420	x	
N8/10	1.944	150.8	23.671	1395	x	
N8/11	1.920	138.7	22.157	1354	x	
N8/12	1.906	139.5	22.266	1357	x	
N8/13	1.893	135.4	21.758	1343	x	
N8/14#	1.940	143.1	22.705	1369	x	
N8/15#	1.876	130.3	21.149	1326	x	
N8/16	1.844	136.0	21.830	1345	x	
N8/17#	1.878	128.5	20.935	1320	x	
N8/18	2.054	189.1	28.688	1523	x	
N8/19	2.051	188.2	28.565	1520	x	
N8/20	2.058	189.4	28.729	1524	x	

TABLE II (continued)

RUN	E _o (volts)	T2 (°F)	P2 (psia)	W _s (ft/s)	DEVICE	
					Osc	TRR
N21/1	1.913	144.6	23.447	1379		x
N21/2	1.943	154.4	24.703	1412		x
N21/3	1.948	158.2	25.206	1425		x
N21/4	1.983	161.8	25.675	1437		x
N21/5	1.946	160.6	25.518	1433		x
N21/6	1.913	148.1	23.900	1391		x
N21/7	1.913	146.1	23.635	1384		x
N21/8	1.941	157.0	25.051	1421		x
N21/9	1.958	154.4	24.703	1412		x
N21/10#	1.912	157.0	25.051	1421		x
N21/11	1.879	139.8	22.848	1363		x
N21/12	1.855	133.6	22.073	1342		x
N21/13+	1.927	134.2	22.146	1344		x

indicates those test runs exhibiting the Mylar burst phenomenon

+ indicates data taken as the hot-wire broke in the shock tube

TABLE III

Actual versus measured air velocity behind incident shock wave.

RUN	V2 _{calc} (ft/s)	V2 _{HW} [*] (ft/s)	DELTA [*] (%)	V2 _{HW} ^{**} (ft/s)	DELTA ^{**} (%)
028/1	358.58	369.53	+3.05	357.58	-0.28
028/2	354.37	387.55	+9.36	364.94	+2.98
028/3#	359.98	387.78	+7.72	364.10	+1.14
028/4	359.98	388.75	+7.99	367.57	+2.11
028/5	359.98	366.77	+1.89	352.11	-2.19
028/6	387.87	403.10	+3.92	390.35	+0.64
028/7	396.18	405.68	+2.40	388.56	-1.92
028/8	400.32	399.00	-0.33	387.04	-3.32
N7/1	367.62	416.36	+13.26	357.84	-2.66
N7/2	346.59	394.91	+13.94	350.68	+1.18
N7/3	340.95	393.72	+15.48	338.97	-0.58
N7/4#	558.33	563.43	+0.91	519.79	-6.90
N7/5#	546.65	559.90	+2.42	522.87	-4.35
N7/6#	554.45	562.23	+1.40	521.43	-5.95
N8/1	605.83	621.26	+2.55	580.07	-4.25
N8/2	607.10	617.62	+1.73	579.46	-4.55
N8/3	618.53	625.07	+1.06	589.81	-4.64
N8/4	558.31	573.83	+2.78	560.69	+0.43
N8/5#	356.36	347.93	-2.37	314.13	-11.85
N8/6	576.38	591.45	+2.61	566.18	-1.77
N8/7	---	---	---	---	---
N8/8	435.02	457.92	+5.26	436.55	+0.35
N8/9	432.30	457.60	+5.85	437.53	+1.21
N8/10	398.08	406.82	+2.20	378.19	-5.00
N8/11	340.88	380.19	+11.53	344.58	+1.09
N8/12	345.11	366.95	+6.33	332.53	-3.64
N8/13	325.29	354.40	+8.95	334.66	+2.88
N8/14#	361.97	400.62	+10.68	358.25	-1.03
N8/15#	301.00	338.82	+12.57	282.58	-6.12
N8/16	328.13	346.23	+5.52	311.99	-4.92
N8/17#	292.36	340.65	+16.52	289.33	-1.03
N8/18	568.65	562.81	-1.03	534.73	-5.97
N8/19	564.78	557.77	-1.24	536.04	-5.09
N8/20	569.94	568.36	-0.28	547.64	-3.91

TABLE III (continued)

RUN	V2 _{calc} (ft/s)	V2 _{HW} [*] (ft/s)	DELTA [*] (%)	V2 _{HW} ^{**} (ft/s)	DELTA ^{**} (%)
N21/1	378.83	381.43	+0.69	374.93	-1.03
N21/2	424.24	425.37	+1.27	422.79	-0.34
N21/3	441.90	436.24	-1.28	430.36	-2.61
N21/4	458.09	484.21	+5.70	482.99	+5.43
N21/5	452.71	437.20	-3.43	438.20	-3.20
N21/6	395.44	384.97	-2.65	380.03	-3.90
N21/7	385.76	382.87	-0.75	383.13	-0.68
N21/8	436.48	426.50	-2.29	425.34	-2.55
N21/9	424.24	442.90	+4.40	436.70	+2.94
N21/10#	436.48	393.96	-9.74	391.77	-10.24
N21/11	356.49	342.60	-3.90	342.18	-4.01
N21/12	326.86	315.32	-3.53	313.94	-3.95
N21/13+	329.70	387.52	+17.54	384.21	+16.53

* indicates "collapsed-linear" reduced data

** indicates "interpolated" reduced data

indicates those test runs exhibiting the Mylar burst phenomenon

+ indicates data taken as the hot-wire broke in the shock tube

TABLE IV

Measured and derived data including Mach, Reynolds, Nusselt, and Prandtl numbers for the conditions behind the incident shock wave.

RUN	M_s	Re	Nu	Pr
028/1	1.206	19.89	2.220	0.688
028/2	1.204	20.79	2.263	0.688
028/3	1.207	20.90	2.264	0.688
028/4	1.207	20.95	2.266	0.688
028/5	1.207	19.77	2.213	0.688
028/6	1.225	22.23	2.301	0.688
028/7	1.230	22.53	2.307	0.688
028/8	1.233	22.24	2.291	0.688
N7/1	1.215	23.27	2.348	0.688
N7/2	1.201	21.68	2.296	0.688
N7/3	1.198	21.51	2.293	0.688
N7/4	1.340	36.87	2.662	0.688
N7/5	1.332	36.29	2.656	0.688
N7/6	1.337	36.67	2.660	0.688
N8/1	1.373	41.77	2.782	0.688
N8/2	1.373	41.56	2.775	0.688
N8/3	1.381	42.45	2.788	0.688
N8/4	1.340	36.87	2.662	0.688
N8/5	1.207	19.04	2.190	0.688
N8/6	1.352	38.83	2.727	0.688
N8/7	---	---	---	---
N8/8	1.258	26.76	2.454	0.688
N8/9	1.256	26.68	2.453	0.688
N8/10	1.234	23.06	2.336	0.688
N8/11	1.197	20.54	2.270	0.688
N8/12	1.200	19.89	2.238	0.688
N8/13	1.188	18.90	2.205	0.688
N8/14	1.211	22.03	2.320	0.688
N8/15	1.173	17.70	2.165	0.688
N8/16	1.190	18.50	2.185	0.688
N8/17	1.167	17.66	2.169	0.688
N8/18	1.347	36.71	2.671	0.688
N8/19	1.344	36.27	2.661	0.688
N8/20	1.348	37.12	2.682	0.688

TABLE IV (continued)

RUN	M_s	Re	Nu	Pr
N21/1	1.222	21.84	2.325	0.688
N21/2	1.251	25.29	2.407	0.688
N21/3	1.263	26.32	2.424	0.688
N21/4	1.273	29.61	2.517	0.688
N21/5	1.270	26.62	2.423	0.688
N21/6	1.233	22.35	2.328	0.688
N21/7	1.226	22.04	2.326	0.688
N21/8	1.259	25.62	2.406	0.688
N21/9	1.251	26.33	2.445	0.688
N21/10	1.259	23.66	2.334	0.688
N21/11	1.208	19.25	2.240	0.688
N21/12	1.189	17.28	2.180	0.688
N21/13	1.191	21.29	2.353	0.688

TABLE V

Turbulence Intensity as a function of air velocity behind the incident shock wave, V_{2HW}^{**} .

RUN	E_{ac} (volts)	E_s (volts)	Turb. Intensity (%)	V_{2HW}^{**} (ft/s)
028/1	0.113	1.922	2.43	357.58
028/2	0.097	1.941	1.75	364.94
028/3#	0.106	1.941	2.09	364.10
028/4	0.122	1.942	2.76	367.57
028/5	0.135	1.919	3.48	352.11
028/6	0.160	1.955	4.62	390.35
028/7	---	1.957	---	388.56
028/8	0.128	1.950	2.96	387.04
N21/1	0.107	1.913	3.07	374.93
N21/2	0.127	1.943	4.06	422.79
N21/3	0.196	1.948	9.52	430.36
N21/4	0.172	1.983	6.96	482.99
N21/5	0.128	1.946	4.04	438.20
N21/6	0.101	1.913	2.71	380.03
N21/7	0.134	1.913	4.80	383.13
N21/8	0.121	1.941	3.67	425.34
N21/9	0.111	1.958	3.05	436.70
N21/10#	0.122	1.912	3.87	391.77
N21/11	---	1.879	---	342.18
N21/12	0.100	1.855	2.98	313.94
N21/13+	1.108	1.927	3.16	384.21

indicates those test runs exhibiting the Mylar burst phenomenon

+ indicates data taken as the hot-wire broke in the shock tube

Bibliography

1. Freymuth, P. "Frequency Response and Electronic Testing of Constant Temperature Hot-Wire Anemometers," J. Phys. E. Sci., Instruments. No. 10, 705, (1977).
2. Gaydon, A.G. and Hurle, I.R. The Shock Tube in High Temperature Chemical Physics. New York: Rinehold Publishing Corp, (1963).
3. Glass, I.I. Shock Tubes, Parts I & II. Toronto: University of Toronto, Institute of Aerophysics, (May 1958).
4. Jones, J.T. Boron Ignition Limit Curve As Determined by a Shock Tube Study. MS Thesis GA/ME/69-1. School of Engineering, Air Force Institute of Technology (AU), Wright-Patterson AFB, OH, (June 1969).
5. King, L.V. "On the Convection of Heat from Small Cylinders in a Stream of Fluid: Determination of the Convective Constants of Small Platinum Wires with Applications to Hot-Wire Anemometry," Pro. Roy. Soc. (London), Vol. 214A, No. 14: 373 (1914).
6. Bradshaw, P. An Introduction to Turbulence and its Measurement. New York: Pergamon Press (1971).
7. Freymuth, P. "A Bibliography of Thermal Anemometry," Thermo-Systems Inc. Bulletin Issue 4, Vol. V, St. Paul, Minnesota (Nov-Dec 1979).
8. Collis, D.D. and Williams, M.J. "Two-Dimensional Convection from Heated Wires at Low Reynolds Numbers," J. Fluid Mech., Vol. 6 (March 1959).
9. Rivir, R.B. Personal communication. AFWAL Aero-Propulsion Laboratories, Wright-Patterson AFB, OH (September 1984).
10. Schlichting, H. Boundary Layer Theory. New York: McGraw-Hill Book Co. (1968).
11. Gude, K.E. and Christoffersen J.A. "The Shock Front Curvature in a Shock Tube Measured with Hot-Wire Anemometers," DISA Information No. 6. Denmark: DISA Elektronik Pub. (1968).

12. Norman, B. "Hot-Wire Anemometer Calibration at High Subsonic Speeds," DISA Information No. 6. Denmark: DISA Elektronik Pub. (June 1967).
13. Chapman, A. and Walker W. Introductory Gas Dynamics. New York: Holt, Rinehart, and Winston, Inc. (1971).
14. Keenan, J.H. and Kaye, J. Gas Tables. New York: John Wiley and Sons (1945).
15. Von Kármán, Th. "Über den Mechanismus des Widerstandes, den ein bewegter Körper in einer Flüssigkeit erzeugt. Nachr. Ges. Wiss. Göttingen, Math. Phys. Klasse (1911-1912).
16. Corrsin, S. "Turbulence: Experimental Methods," Handbuch der Physik, Vol. 8 Part 2, Springer, Berlin (1963).
17. Roshko, A. "On the Development of Turbulent Wakes From Vortex Streets," NACA TR 1191 (1954).
18. Roshko, A. "Experiments on the Flow Past a Circular Cylinder at Very High Reynolds Number," Journal of Fluid Mechanics, Vol. 10 (1961).
19. Morkovin, M.V. "Flow Around Circular Cylinder - A Kaleidoscope of Challenging Fluid Phenomena," Symposium On Fully Separated Flows, ASME. New York (1964).
20. Beckwith, T.G. and Buck, N.L. Mechanical Measurements. Massachusetts: Addison-Wesley Publishing Co. (1969).
21. Fertis, D.G. Dynamics and Vibrations of Structures. New York: John Wiley and Sons, Inc. (1973).
22. Mierovitch, L. Elements of Vibration Analysis. New York: McGraw-Hill, Inc. (1975).

Vita

Captain Stephen M. McQueen was born on 10 March 1956 at Bergstrom AFB, Austin, Texas. He graduated from high school in Blythville, Arkansas in 1974 and attended the University of Texas at Austin from which he received the degree of Bachelor of Science in Aerospace Engineering in December 1979. Upon graduation, he received a commission in the USAF through the ROTC training program and entered active duty service in January 1979. Captain McQueen's first assignment was as a Research and Development Munitions Test Engineer at Eglin AFB, Florida, where he tested air-to-ground bombs, dispensers, and mines until 1982. From 1982-1983 he worked as a Programming Engineer at Eglin AFB until he entered into a Master of Science program in Aeronautical Engineering at the Air Force Institute of Technology at Wright-Patterson AFB, Dayton, Ohio.

100-100000-1

100-100000-1

100-100000-1

END

FILMED

7-85

DTIC